

# Water at polar and nonpolar solid walls (Review)

Felix Sedlmeier

*Physik Department, Technische Universität München, 85748 Garching, Germany*

Jiri Janecek

*Physik Department, Technische Universität München, 85748 Garching, Germany and Institute of Physical and Applied Chemistry, Brno University of Technology, Purkyňova 118, 61200 Brno, Czech Republic*

Christian Sendner

*Physik Department, Technische Universität München, 85748 Garching, Germany*

Lyderic Bocquet

*Physik Department, Technische Universität München, 85748 Garching, Germany and Laboratoire de Physique de la Matière Condensée et Nanostructures, CNRS and Université de Lyon, 43 Boulevard du 11 Novembre 1918, 69622 Villeurbanne, France*

Roland R. Netz and Dominik Horinek<sup>a)</sup>

*Physik Department, Technische Universität München, 85748 Garching, Germany*

(Received 25 July 2008; accepted 23 September 2008; published 3 November 2008)

Recent progress in simulating the properties of interfacial water at hard hydrophobic and hydrophilic surfaces is reviewed and compared to results for the air/water interface. The authors discuss static properties such as the equilibrium contact angle, the depletion layer thickness, and the orientation of interfacial water molecules. Relations between these properties, e.g., the relation between the contact angle and the thickness of the depletion layer which is experimentally observed on hydrophobic surfaces, are emphasized. For a hydrophilic sapphire surface, the authors discuss the influence of geometry and density of polar surface groups on the interfacial water structure. They discuss nonequilibrium effects arising in laminar shear flows, where the classic no-slip hydrodynamic boundary condition is violated at hydrophobic interfaces. They discuss the arising slip and relate it to static properties of the solid hydrophobic/water interface. © 2008 American Vacuum Society. [DOI: 10.1116/1.2999559]

## I. INTRODUCTION

Water is by far the most important liquid in biology and in industrial or technological applications.<sup>1</sup> In its bulk phase, it shows many anomalies,<sup>2</sup> which are believed to be related to the ability of water molecules to form a strong hydrogen bonding network. It comes at no surprise that water also shows quite special behavior when it interacts with other matters. This includes the properties of water as a solvent, where especially the hydrophobic solvation of nonpolar molecules,<sup>3–5</sup> which has gained extensive attention mainly in the context of protein folding,<sup>6</sup> shows anomalous behavior,<sup>7,8</sup> as well as water in an extended interfacial geometry, which is the topic of this overview.

The simplest extended interface is liquid water in contact with its vapor phase. At ambient conditions, the density of the vapor phase is so low that only interactions within the liquid phase determine the surface properties. The high affinity of water molecules for themselves gives rise to a very high surface tension of 72 mN/m at room temperature,<sup>9</sup> which is only surpassed by liquid mercury.<sup>10</sup> The air/water interface also exhibits a surface potential, the magnitude and sign of which have been disputed.<sup>11,12</sup>

For interfaces of water with a solid phase, the interactions are more complex. Similar to the air/water interface, the at-

traction between water molecules is a key factor of the interfacial energetics but is amended by the water-surface interactions. There is a large variety of solid substrates with rather different surface characteristics. Besides the exact chemical nature of the substrate, which governs the detailed water-surface interactions, a general classification of the substrate is given by the hydrophobicity, i.e., the affinity of water to contact the surface. It is quantified by the contact angle that a droplet of water forms on the surface.<sup>13</sup> This contact angle ranges from 180° at air to 0° for very hydrophilic materials, where droplets of water spread on the surface, and a contact angle cannot be determined anymore. Hydrophobicity is observed for nonpolar surfaces, where the interactions among the water molecules themselves exceed the water-surface interactions.<sup>14</sup> For very nonpolar surfaces, contact angles of up to approximately 130° can be obtained.<sup>15</sup> Higher contact angles belong to the “superhydrophobic” regime and cannot be achieved by chemical modification of the surface character but by nanoscopic structuring of the surface.<sup>16</sup>

The necessity of the absence of polar surface groups limits the chemical diversity of hydrophobic surfaces. The most common chemical structure of hydrophobic substrates is a hydrocarbon motif. Because of the similar electronegativity of carbon and hydrogen, the CH bond is only weakly polarized. With the advance of self-assembled monolayer technology, nowadays it is possible to cover a great variety of surfaces, e.g., different metals and vitreous glass, with a sheet of

<sup>a)</sup>Electronic mail: dominik.horinek@ph.tum.de

hydrophobic alkane chains.<sup>17,18</sup> Other hydrophobic materials are graphite,<sup>19</sup> hydrogen-terminated diamond,<sup>20</sup> and fluorinated hydrocarbons.<sup>21</sup>

A remarkable observation at solid hydrophobic/water interfaces is the reduced density in the interfacial region compared to the density in the bulk solid and water, which is seen in scattering experiments.<sup>22–26</sup> In theoretical studies, it was predicted by analytical theories<sup>27,28</sup> and by atomistic simulations.<sup>29–31</sup> The physical origin of this depletion is still under discussion.<sup>32</sup>

Another interesting manifestation of hydrophobicity at solid surfaces is their behavior in hydrodynamic flows. For usual surfaces, a lateral flow of a liquid is described by the Navier–Stokes equation in conjunction with the “no-slip” boundary condition, which implies that the interfacial fluid layer is at rest relative to the surface. For a flow of water along a hydrophobic material, this boundary condition is violated, and the interfacial water layer moves relative to the surface.<sup>33–36</sup> This slippage effect has important implications in fluid technology because it gives a drastic increase in the flow rate through nanofluidic devices.<sup>37</sup>

Hydrophilic surfaces are much more abundant in nature. There is a much larger variety of chemical motifs and an even nearly exhaustive account cannot be given in this paper. Just to name a few, polar surfaces such as biological membranes, surfaces of ionic crystals, charged surfaces, or metallic surfaces, which attract polar water molecules through the inductive force, all possess hydrophilic surface character, i.e., a contact angle of less than 90°.

Theoretical studies of interfaces involving liquid water is a difficult task. The calculation of minimum potential energy structures does not correspond to the observed structures of the liquid because entropic contributions to the free energy are important. Furthermore, large systems need to be considered since cooperative effects in the liquid phase contribute to the water behavior. This inevitably leads to complicated statistical mechanical problems for which realistic solutions are not analytically possible. As an illustration of the complexity of aqueous surfaces, we note that two simple models for the air/water interface gave opposing signs of the surface potentials.<sup>38,39</sup> For this reason, the air/water interface has been subject of molecular simulations for more than 20 years.<sup>40–42</sup> Atomistic computer simulations, either by molecular dynamics or by Monte Carlo, take advantage of numerical algorithms for a prediction of the behavior of the system of interest within an approximate model for the interaction energy. Thus, they allow studies of complex, high-dimensional systems without restricting the degrees of freedom involved. On the other hand, the usage of classical force fields that most often are simply pairwise additive and involve fitted force field parameters constitutes a whole set of hidden assumptions, the reliability of which is in practice difficult to assess.

The simulation study of water in contact with solid surfaces has very early attracted considerable attention. Already in 1984, Lee *et al.*<sup>43</sup> reported their seminal study of water at the interface to a model hydrophobic surface, which was

later extended to hydrophilic surfaces.<sup>44</sup> There have been many simulations of water in contact with various surfaces reported. These include studies of water in contact with structureless walls,<sup>45–47</sup> metals,<sup>48–51</sup> ionic crystals,<sup>52</sup> lipid membranes,<sup>53–56</sup> self-assembled monolayers,<sup>57–59</sup> clay minerals,<sup>60</sup> and many others. In this paper, we present results for hydrophobic, hydrogen-terminated diamond, as well as for different idealized models of hydrophilic surfaces and sapphire. In our analysis, we focus on structural effects at these surfaces, electrostatic properties, wetting behavior, and on the solvent-flow response to shear. In Sec. II we describe all methods and surfaces we investigate. In Secs. III–V we present results for the air/water interface, for solid hydrophobic/water interfaces, and for solid hydrophilic/water interfaces. Section VI gives a summary and outlook.

## II. METHODS

### A. Monte Carlo and molecular dynamics simulations

We employ two different types of simulation methods, Monte Carlo (MC) and molecular dynamics (MD), for the study of the interface of water with air and with different solids. In MD,<sup>61</sup> Newton’s equations of motion are numerically integrated, whereas in MC,<sup>61</sup> canonical distribution functions are directly evaluated by stochastic methods. For the generation of ensembles for the study of static properties, MD does not offer any real advantage over MC, and a MC calculation is in principle more efficient. In contrast, the study of time-dependent phenomena such as a shear flow requires the explicit treatment of the particle momenta, and MC simulations are no longer applicable. In our MC and MD simulations of interfaces, all calculations are carried out in a rectangular box with periodic boundary conditions applied along all three directions. The simulation box is partly filled by the water phase, which forms a continuous slab along the  $xy$ -plane. In the  $z$ -direction, only part of the box is occupied by the water phase, and the rest of the box is either empty, producing a model air/water interface or filled by the solid, in which case a solid/water interface is formed. Depending on the thickness of the film such a system represents either a model for a simple solid/water interface or for water in a slitlike nanopore.

For any simulation study of liquid water, the choice of the water model is crucial. Our simulations are based on the simple point charge (SPC) (Ref. 62) and extended simple point charge (SPC/E) (Ref. 63) water models, whose force field parameters are listed in Table I. These two simple models have the simplicity of a nonpolarizable three-site water model and have been successfully applied to the study of water in interfacial geometries.<sup>29,30</sup> Of similar importance is the choice of water-solid interactions. A detailed discussion of the interaction parameters for every distinct surface will be given at the end of Sec. II.

The MD simulations are carried out with the GROMACS (Ref. 64) package. The simulations are done at 300 K in the  $NVT$  (constant particle number, volume, and temperature) ensemble for the air/water interface and in the  $NP_{\mu}AT$  (con-

TABLE I. Force field parameters of the SPC (Ref. 62) and SPC/E (Ref. 63) water models;  $q_i$ ,  $\varepsilon_i$ , and  $\sigma_i$  are the partial charge and Lennard-Jones interaction parameters of atom type  $i$ ,  $b_0$  is the bond length, and  $\theta_0$  is the angle between the two OH bonds. The hydrogen atoms do not interact via a Lennard-Jones interaction.

	SPC	SPC/E
$\varepsilon_O$ (kJ/mol)	0.6502	0.6502
$\sigma_O$ (Å)	3.166	3.166
$q_O$ (e)	-0.82	-0.8476
$q_H$ (e)	0.41	0.4238
$b_0$ (Å)	1.0	1.0
$\theta_0$ (deg)	109.47	109.47

stant particle number, vertical pressure, surface area, and temperature) for the solid/water interfaces. The temperature control is achieved by either a Langevin thermostat with an inverse friction constant of  $\gamma^{-1}=1.0$  ps or by a Berendsen weak coupling thermostat with a relaxation time between 0.4 and 1 ps. The pressure coupling in the  $NP_zAT$  simulations is achieved by a weak coupling barostat with a relaxation time of 1.0 ps. All nonbonded interactions are cut off at the cutoff distance  $r_c$  of 8 Å in the molecular dynamics simulations. Periodic boundary conditions are applied in all three directions and long-range electrostatic interactions are treated by particle mesh Ewald summation<sup>65</sup> with tinfoil boundary conditions. The real space part of the electrostatic interactions is cut off at the cutoff distance  $r_c=8$  Å and the grid spacing for the reciprocal part is chosen as 1.2 Å. All bonds involving hydrogen atoms are constrained using the LINCS (Ref. 66) or SHAKE (Ref. 67) algorithm (in the substrates) or the analytic SETTLE algorithm<sup>68</sup> (in the water molecules), and a time step of 2 fs is used for the integration of the equations of motion.

The Monte Carlo simulations are also performed in the  $NP_zAT$  ensemble using a self-written code. A randomly chosen particle (either a water molecule or a flexible group of the surface) is translated and rotated in order to obtain a new configuration which is accepted or rejected according to the standard acceptance criteria. The maximal translational and rotational displacements are in the ranges of 0.15–0.25 Å (along each axis  $x$ ,  $y$ , and  $z$ ) and 0.1–0.3 rad for each of the three angles characterizing the molecular orientation; these values lead to acceptance ratios between 15% and 30%. The changes in the volume of the simulation box are done once in every MC cycle (one MC cycle corresponds to an attempt to move every particle in the box which is allowed to move). Every simulation is 50 000 MC cycles long which corresponds approximately to  $100 \times 10^6$  configurations in the case of sapphire simulations, where 2000 water molecules are present. The variant of the Ewald summation technique as described by Yeh and Berkowitz<sup>69</sup> is employed to treat the electrostatic interactions. The recommended value of the damping parameter  $\alpha=5.6$  is taken and the contribution in the reciprocal space is summed for all vectors with  $(k_x, k_y, k_z) \leq (5, 5, 10)$ . In the MC simulations, the real space part, as well as the Lennard-Jones interactions, is truncated at

$r_c=12.5$  Å and an inhomogeneous correction to the dispersion contribution to the energy and the components of the virial tensor is added.<sup>70</sup>

## B. Methods of analysis

### 1. Density profiles and depletion layer

From the simulation results, various structural quantities are accessible, the simplest of which is the mass density  $\rho$ . In an interfacial, inhomogeneous system, the density is a function of the  $z$ -coordinate, which is normal to the interface. We calculate the profiles of the density of every component  $i$ ,  $\rho_i(z)$ , as a function of the  $z$ -coordinate. The density of component  $i$  in the system at position  $z_0$  is the average density of atoms belonging to molecules of type  $i$  in a finite slice along the  $z$ -coordinate with center  $z_0$  and width  $\Delta z$ .

For the air/water interface, we use the position  $z_{\text{GDS}}$  of the Gibbs dividing surface (GDS) as the origin of  $z$ . The GDS is the natural boundary of the aqueous phase, for which the surface excess of the water itself vanishes,

$$\int_{-\infty}^{z_{\text{GDS}}} \rho_{\text{wat}}(z) dz + \int_{z_{\text{GDS}}}^{\infty} [\rho_{\text{wat}}(z) - \rho_{\text{wat}}^{\text{bulk}}] dz = 0. \quad (1)$$

For the solid/water interfaces, we choose the position of the outermost layer of surface atoms as the origin of  $z$ . The thickness of the depletion layer  $d_l$  is defined as the density deficit integrated over the whole interfacial region,

$$d_l = \int_{-\infty}^{\infty} \left[ 1 - \frac{\rho_1(z)}{\rho_1^b} - \frac{\rho_2(z)}{\rho_2^b} \right] dz, \quad (2)$$

where  $\rho_1(z)$  and  $\rho_2(z)$  are the density profiles of the two phases at contact and  $\rho_1^b$  and  $\rho_2^b$  denote the respective bulk values. The quantity  $d_l$  corresponds to the thickness of a virtual gap between two phases and can be directly estimated from neutron reflectivity experiments.<sup>22,25</sup>

### 2. Charge density profile and electrostatic potential

Analogous to the mass density profile, the profiles of the charge density  $\rho_{\text{el}}$  and the mean dipole angle  $\langle \cos(\xi) \rangle$  of the water molecules are calculated from the particle positions. The electric field along  $z$ ,  $E_z(z)$  and the electrostatic potential  $\Phi(z)$  are important characteristics of the interface. They are obtained by integrating Poisson's equation twice, where  $\varepsilon_0$  is the vacuum permittivity,

$$E_z(z) = \int_{-\infty}^z \frac{\rho_{\text{el}}(z')}{\varepsilon_0} dz', \quad (3)$$

$$\Phi(z) = - \int_{-\infty}^z E_z(z') dz'. \quad (4)$$

### 3. Orientation distributions

Closely related to the appearance of a net electrostatic potential is the average orientation of the interfacial water molecules. The orientation of a water molecule can be specified by the angles  $\tau$  and  $\xi$ , where  $\tau$  is the angle between an

OH vector of a water molecule and the surface normal. Thus, for every water molecule two values of  $\tau$  are obtained. The angle  $\xi$  is the angle between the water molecules dipole moment and the surface normal. The surface normal vector is defined as pointing toward the water phase. Figure 1 shows orientations of water molecules for representative values of  $\tau$  and  $\xi$ . The orientation of the water molecules near an interface is determined by the joint angular probability distribution  $P[\cos(\tau), \cos(\xi)]$  relative to the distribution of an isotropic system. The joint distributions contain the full orientational information and provide insights that cannot be seen in the one-dimensional probability distributions for ei-

ther angle. We divide the simulation box into slices parallel to the interface and calculate  $\cos(\tau)$  and  $\cos(\xi)$  by taking the scalar product of the normalized OH and dipole vectors with the surface normal vector. The water molecule orientations are then analyzed on a  $50 \times 50$  grid for  $\cos(\tau)$  and  $\cos(\xi)$ , which corresponds to a bin size of  $0.04 \times 0.04$ . The count in each bin is divided by the number of molecules in the bin that is expected for an isotropic distribution, which is obtained by integrating the analytic isotropic distribution  $P_0$  [see Eq. (5)] over the corresponding bin. In Eq. (5),  $\alpha = 109.47^\circ$  is the angle between the two OH vectors in a SPC/E water molecule,

$$P_0[\cos(\tau), \cos(\xi)] = \left[ 2\pi \sqrt{\sin^2 \frac{\alpha}{2} - \cos^2 \xi - \cos^2 \tau + 2 \cos \xi \cos \tau \cos \frac{\alpha}{2}} \right]^{-1}. \quad (5)$$

Thus,  $P[\cos(\tau), \cos(\xi)]$  gives the probability of finding a water molecule in the specified orientation relative to the probability  $P_0$  to find the molecule in the same orientation in the isotropic case. The results are plotted as two-dimensional contour plots against  $\cos(\tau)$  and  $\cos(\xi)$ , where the brightness corresponds to the probability  $P[\cos(\tau), \cos(\xi)]$ . In Fig. 1, we indicate the orientation of a water molecule corresponding to different points in the  $\cos(\tau)$ – $\cos(\xi)$  plane by the water molecules placed at these points in the plot. One-dimensional probability distributions as a function of  $\cos(\tau)$  or  $\cos(\xi)$  are obtained by integrating over the other coordinate in the joint distributions.

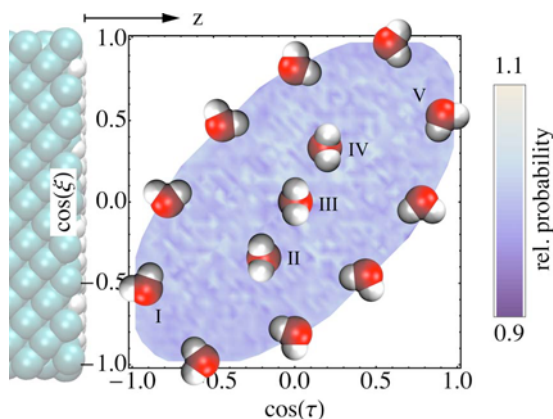


FIG. 1. Illustration of several typical orientations of water molecules with respect to the water interface corresponding to different positions in the  $\cos(\tau)$ – $\cos(\xi)$ -plane. Here  $\tau$  is the angle between the OH vectors of a water molecule and the surface normal, and  $\xi$  is the angle between the water molecule dipole and the surface normal. In the background the orientational distribution from an actual water simulation in the bulk is shown, which exhibits a rather uniform distribution within an ellipse corresponding to the possible combinations of  $\tau$  and  $\xi$ .

#### 4. Interfacial tension, wetting coefficient, and contact angle

The wetting coefficient  $k$  and the contact angle  $\theta$  (see Fig. 2),  $k = \cos \theta$ , are the basic quantities characterizing the mutual affinity between the liquid and the solid substrate. They are calculated from the simulation data according to two different protocols. The first method employs Young's equation

$$k = -\frac{\gamma_{LS} - \gamma_{SV}}{\gamma_{LV}}, \quad (6)$$

where  $\gamma_{LS}$  is the interfacial tension between solid and liquid phase,  $\gamma_{LV}$  is the surface tension of the liquid, and  $\gamma_{SV}$  is the surface free energy of the solid phase. If the solid is frozen, then  $\gamma_{SV}$  can be neglected, and the remaining two interfacial tensions can be calculated within the simulations of appropriate systems as the difference between diagonal components of the virial tensor according to

$$\gamma_{\alpha\beta} = \frac{1}{2S} [2\Pi_{zz} - (\Pi_{xx} + \Pi_{yy})], \quad (7)$$

where  $S$  is the surface area of the interface (cross section of the simulation box) and  $\Pi_{xx}$ ,  $\Pi_{yy}$ , and  $\Pi_{zz}$  are the components of the virial tensor.

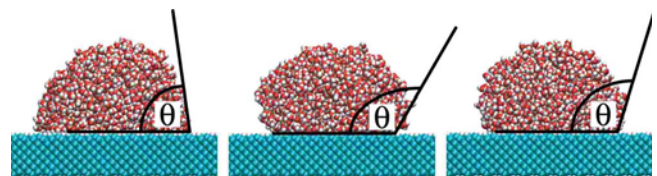


FIG. 2. Representative snapshots of a simulation of a water droplet containing 2000 water molecules on a hydrophobic diamond surface modeled with a water-surface Lennard-Jones interaction strength of  $\epsilon_{LS} = 0.42$  kJ/mol. Also shown is the instantaneous contact angle  $\theta$ . The average contact angle on this surface is  $\theta_{mic} = 107^\circ$ .

This approach was first used by Jensen and co-workers<sup>71,72</sup> for studies of water confined between hydrophobic (alkane) and hydrophilic (alcohol) surfaces, where a contact angle of  $\theta=112^\circ$  was obtained on the hydrophobic surface. Pertsin and Grunze<sup>73</sup> used a similar approach for water at a graphite surface, where they froze all coordinates of the solid. Thus, internal interactions within the solid do not contribute to the surface tension, giving an increased numerical accuracy. Recently, an analogous method was used to investigate the relation between the wetting coefficient and the depletion thickness for various model substrates.<sup>26,30</sup>

The second method is the direct simulation of the contact angle. In this method, a nanoscale water droplet on a substrate surface is simulated by molecular dynamics and the contact angle is extracted from the droplet's shape.<sup>19</sup> Initially, a rectangular block of SPC/E water molecules that has been equilibrated previously is placed on top of the surface. After equilibration, the droplet assumes a roughly spherical shape, but exhibits pronounced shape fluctuations. It is therefore simulated for several nanoseconds to obtain a sufficiently long trajectory for statistical analysis. In Fig. 2 we show three representative snapshots of a droplet on a diamond surface with a solid-liquid Lennard-Jones parameter of  $\epsilon_{LS}=0.42$  kJ/mol. It is seen that the instantaneous contact angle shows large variations between different snapshots. For the determination of the contact angle from the MD trajectories, we apply a procedure described by de Ruijter *et al.*<sup>74</sup> For the definition of the droplet's contour, we divide the box into slices of 0.5 Å thickness parallel to the surface and calculate the radial density profile for each slice, with its center at the center of mass of the droplet. The GDS is determined for each slice by fitting the density profile to the function,<sup>19</sup>

$$\rho(r) = \frac{1}{2}\rho^l \left\{ 1 - \tanh \left[ \frac{2(r - r_{\text{GDS}})}{d} \right] \right\}, \quad (8)$$

where  $\rho(r)$  is the radial density profile,  $r_{\text{GDS}}$  is the position of the GDS, and  $d$  is a measure for the thickness of the interface. It has been argued that an error function is the correct fitting function,<sup>75,76</sup> but in order to stay close to Ref. 19 we use a tanh function. The fit is sufficiently good, and the selection of either an erf or a tanh will have rather little influence on the resulting contact angles. We extract the contact angle by extrapolating a circular fit of the contour line to the diamond surface, which is defined by the  $z$ -position of the outermost atom layer. We discard all points with a distance to the surface of less than 8 Å to avoid artifacts that are due to strong density fluctuations at the liquid-solid interface. Furthermore, only those points are taken into account for which the radial density profile reaches a plateau of more than 0.5 kg/l in the center of the droplet, thus excluding the "pole" region of the droplet where the statistics is poor. We apply this analysis during successive time intervals of 500 ps and continue the simulation until the contact angles are converged, after typically 5–10 ns.

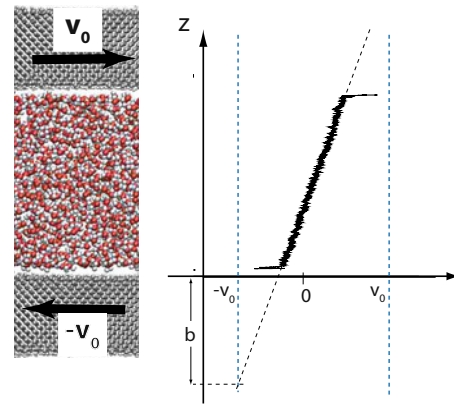


FIG. 3. Snapshot of the water-diamond system used in the shearing simulations with 4 nm gap size (left). Not shown is the second water film. The diamond slab is 1.5 nm thick and has  $3.0 \times 3.0$  nm<sup>2</sup> lateral extension. On the right, the solvent velocity profile for shearing velocity  $v_0=0.02$  nm/ps is shown, giving rise to a slip length  $b$ . The vertical broken lines denote the surface velocity  $\pm v_0$ .

For microscopic droplets, the effects of the line tension on the contact angle cannot be neglected. The macroscopic contact angle  $\theta$ , which is the observable in common experiments, and the microscopic contact angle  $\theta_{\text{mic}}$ , which is obtained in molecular simulations, are related by<sup>19</sup>

$$\cos \theta = \cos \theta_{\text{mic}} + \frac{\sigma}{\gamma_{LV} r_b}, \quad (9)$$

where  $\sigma$  is the line tension,  $\gamma_{LV}$  is the liquid-vapor interfacial tension, and  $r_b$  is the radius of the roughly circular contact area between the droplet and the surface. Thus, the effect of the line tension can be estimated by simulating droplets of different sizes and plotting the resulting  $\cos \theta_{\text{mic}}$  as a function of  $1/r_b$ . This yields a linear relation that can be extrapolated to  $1/r_b=0$ , where the macroscopic contact angle  $\cos \theta$  is obtained.

We explicitly performed this extrapolation for one set of carbon-carbon parameters: Lennard-Jones radius  $\sigma_C = 3.58$  Å and interaction strength  $\epsilon_{LS}=0.42$  kJ/mol with three water droplets of 1000, 2000, and 4000 water molecules. We found contact angles of  $\theta_{\text{mic}}=109.8^\circ$ ,  $107.1^\circ$ , and  $106.0^\circ$  and base radii of  $r_b=2.0$ , 2.6, and 3.4 nm for droplet sizes of 1000, 2000, and 4000 water molecules. The linear extrapolation yields a macroscopic contact angle of  $\theta=100.7^\circ$  and a line tension of  $\sigma=0.17 \times 10^{-10}$  J/m, where  $\gamma_{LV}=52.7$  mN/m has been used. For all other surfaces, this effect was ignored and droplets of 2000 water molecules were used.

## 5. Shear flow simulations

We use nonequilibrium molecular dynamics simulations to examine sheared water layers confined between different hydrophobic hydrogen-terminated diamond slabs. The system consists of two diamond blocks that are separated by two SPC/E water slabs of thickness  $Z \approx 4$  nm. In Fig. 3(a), we show a snapshot of the simulation system, where only one of the water slabs is shown.

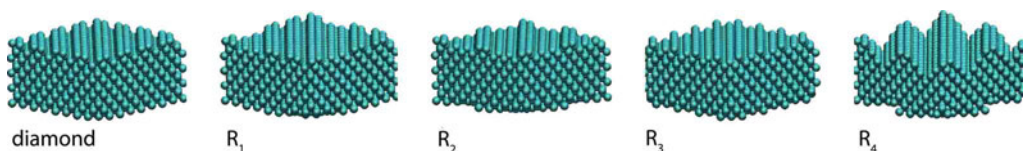


FIG. 4. Diamond surface structures used in the simulations. The surfaces are ordered by increasing roughness.

A Couette shear flow is induced by attaching harmonic springs with spring constant  $k=1000 \text{ kJ mol}^{-1} \text{ nm}^{-2}$  to the upper and lower surfaces, and pulling the lower spring with a velocity  $v_{\text{surf}}=v_0$  in the  $x$ -direction and the upper spring with  $v_{\text{surf}}=-v_0$  such that the net momentum vanishes.

The movement of the diamond surfaces creates a linear velocity profile for the solvent flow [see Fig. 3(b)]. Using the definition of a partial slip boundary condition at the position of the surface,

$$|v_{\text{surf}}| - |v_x|_{z=z_{\text{surf}}} = b \left| \left( \frac{\partial v_x}{\partial z} \right)_{z=z_{\text{surf}}} \right|, \quad (10)$$

the slip length  $b$  is obtained by extrapolating the velocity profile. For that purpose, the velocity profile is fitted to a linear function. In the simulation cell, there are four liquid/solid interfaces, leading to four slip lengths. Error bars are given in terms of their standard deviation.

The systems are equilibrated for 200 ps and then subsequent production runs of up to 30 ns are performed. Several simulations with the same parameters are performed and all trajectories are used for the further analysis.

The used Berendsen weak-coupling thermostat is in principle critical for shear simulations, and it needs to be demonstrated that it does not influence the resulting slip lengths from shear flow simulations. This issue has been checked by performing two benchmark simulations, where a Berendsen thermostat scaling the velocity in all Cartesian directions and a Nosé-Hoover thermostat with velocity scaling only in the  $y$ -direction are applied during otherwise identical simulations.<sup>77</sup> We found no difference between these different simulation protocols.

### C. Surfaces

For our study of the solid/water interface we use polar and nonpolar substrates. The nonpolar surface is hydrogen-terminated diamond, as polar surfaces idealized solid substrates with terminal OH groups<sup>30</sup> and a model sapphire surface are used.

#### 1. Diamond

The diamond surface is modeled by the well known double face-centered-cubic lattice (lattice constant  $a=3.567 \text{ \AA}$ ) of C atoms with the  $\langle 100 \rangle$  direction parallel to the  $z$ -axis. A slab of finite thickness is cut out of the lattice with its two surfaces perpendicular to the  $z$ -axis, and the surface layer is reconstructed and terminated by H atoms in order to represent an ideal hydrophobic surface. The atoms of the diamond interact with each other via harmonic bond

and angle potentials as well as a torsion potential. The force constants are taken from the GROMOS96 force field.<sup>78</sup> The interaction between a surface carbon atom and a water oxygen atom at distance  $r_{ij}$  is given by the Lennard-Jones potential,

$$V_{LS}(r_{ij}) = 4\epsilon_{CO} \left[ \left( \frac{\sigma_{CO}}{r_{ij}} \right)^{12} - \left( \frac{\sigma_{CO}}{r_{ij}} \right)^6 \right]. \quad (11)$$

The potential depth  $\epsilon_{CO}$ , which is equal to  $\epsilon_{LS}$  in our case, and the interaction length  $\sigma_{CO}$  are calculated by geometric combination rules,

$$\sigma_{CO} = \sqrt{\sigma_C \sigma_O}, \quad (12)$$

$$\epsilon_{CO} = \sqrt{\epsilon_C \epsilon_O}. \quad (13)$$

For tuning the hydrophobicity of the diamond surface, the interaction strength between the water molecules and the surface atoms is varied by adjusting the carbon-water interaction strength  $\epsilon_{CO}$  in the range of 0.11-0.72 kJ/mol, whereas the C-O interaction length  $\sigma_{CO}=3.37 \text{ \AA}$  is held constant. The range of  $\epsilon_{CO}$  is chosen such that the default value of the GROMOS96 force field ( $\epsilon_{CO}=0.42 \text{ kJ/mol}$ ) is roughly in the center of the studied range.

The surface is frozen during most of the simulations, i.e., the position of all atoms is held fixed. In most simulations the diamond slab is 1.5 nm thick and has a lateral extension of  $3.0 \times 3.0 \text{ nm}^2$ . Only for the direct contact angle measurements a larger slab of  $12.0 \times 12.0 \text{ nm}^2$  with the same thickness is used.

#### 2. Rough surfaces

For studying the effect of surface roughness on the slip length appearing in a Couette flow, we use diamond surfaces with different degrees of nanoroughness. These surfaces are constructed by setting the interaction between selected surface atoms and all water molecules to zero. The different surface structures are shown in Fig. 4. Surface R1 is constructed by erasing every third pair of rows of surface atoms, and surface R2 is obtained by deletion of every second pair of rows. For the construction of R3, every second single row of carbon atoms is deleted, and the roughest surface, R4, is generated by removing carbon atoms down to the fourth surface layer of carbon atoms. Again, deletion of a surface atom merely means that  $\epsilon_{CO}$  is set to zero for this distinct atom.

#### 3. Hydrophilic model surfaces

In Ref. 30 several idealized models of hydrophilic solid substrates were used. Rigid regular lattices of interaction

sites that interact with the SPC/E water molecules through Lennard-Jones interactions only (which should model e.g., the methylene groups in a polyethylene crystal or in alkane self-assembled monolayers) were constructed. The geometry of the lattice was either hexagonal or tetragonal with lattice constants of  $a=4.3832 \text{ \AA}$  and  $c=1.4775 \text{ \AA}$  (tetragonal case) or  $c=1.60 \text{ \AA}$  (hexagonal case). In the topmost layer, a variable fraction of sites  $x_{\text{OH}}$  was replaced by hydroxyl groups (OH) for tailoring the hydrophilicity of the substrates. For the tetragonal lattice surface fractions of  $x_{\text{OH}}=0, 1/2, \text{ and } 1$  were studied, and for the hexagonal case the surface fractions were  $x_{\text{OH}}=0, 1/3, 2/3, \text{ and } 1$ . For both surfaces the OH groups were regularly distributed over the surface, leading to a surface density of OH groups,  $\xi_{\text{OH}}$ , of up to  $0.06 \text{ \AA}^{-2}$ . The inclination angle  $\delta$  between the OH vector and the surface normal has been varied systematically between  $0^\circ$  and  $135^\circ$ . For the Lennard-Jones interactions of the nonpolar sites the optimized potentials for liquid simulations (OPLS) parameters for a methylene group,<sup>79</sup>  $\epsilon_{\text{CC}}=0.4938 \text{ kJ/mol}$  and  $\sigma_{\text{CC}}=3.905 \text{ \AA}$ , were used, and the interactions of the OH groups were modeled by the OPLS parameters for aliphatic alcohols,<sup>80</sup> in which the Lennard-Jones interaction is centered on the oxygen atoms with  $\epsilon_{\text{OO}}=0.7115 \text{ kJ/mol}$  and  $\sigma_{\text{OO}}=3.07 \text{ \AA}$ . Partial charges of  $q_{\text{H}}=+0.435e$ ,  $q_{\text{O}}=-0.700e$ , and  $q_{\text{C}}=+0.265e$  have been assigned to the OH hydrogen, the OH oxygen, and the neighboring methylene group.

#### 4. Sapphire surface

The behavior of water at the (0001) surface of sapphire is studied. In this notation, the first, second, and fourth Miller indices give the reciprocal values of the intersections of the crystallographic plane with the  $x$ -,  $y$ -, and  $z$ -axes, and the third one is the sum of the first two. It was shown by experimental and theoretical approaches that even the humidity in air induces complete coverage of this surface by OH groups.<sup>81</sup> The top view of a part of this surface is shown in Fig. 5. The depicted hexagonal cluster was optimized using density functional theory (DFT) quantum chemistry methods;<sup>82</sup> for our purposes this cluster is periodically replicated in the  $xy$ -plane and a rectangular block with lateral size of  $35.4309 \times 34.0925 \text{ \AA}^2$  is cut out. The solid substrate is treated as a single layer of Al atoms with the respective number of oxygen atoms pointing toward the solid side and OH groups pointing toward the water side. The total sum formula is  $\text{Al}_{312}\text{O}_{358}(\text{OH})_{266}$ .

For the partial charges of the atoms comprising the sapphire lattice, the following average values deduced from the DFT calculations were used:  $q_{\text{Al}}=+1.926e$ ,  $q_{\text{H}}=+0.516e$ , and  $q_{\text{O}}=-1.1832e$  for both types of oxygen atoms. The Lennard-Jones parameters for O and H sites were identical with those for SPC/E water ( $\sigma_{\text{O}}=3.166 \text{ \AA}$  and  $\epsilon_{\text{O}}=0.65 \text{ kJ/mol}$ ). Since there is no interaction potential model optimized for SPC/E water interacting with aluminum in sapphire we employed *ad hoc* estimates  $\sigma_{\text{Al}}=2.86 \text{ \AA}$  and  $\epsilon_{\text{Al}}=0.46 \text{ kJ/mol}$  for the aluminum-water Lennard-Jones interactions. This is a very crude modeling, but we believe that the influence of the Lennard-Jones interactions of the buried

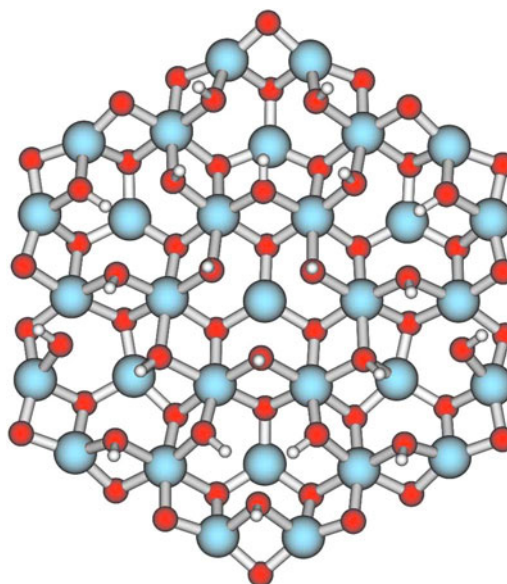


FIG. 5. Structure of the (0001) surface of sapphire with a monomolecular layer of bound hydroxyl groups.<sup>82</sup> White spheres represent hydrogen atoms, black spheres oxygen atoms, and gray spheres aluminum atoms.

Al atoms is of little importance. The precise structure of the layer of bound hydroxyl groups is the subject of ongoing studies and we employed two simplified models. In the first model, labeled S1, we assume that 66% of the OH groups are pointing directly into the water phase (inclination angle  $\delta=0^\circ$ ), and that the remaining 34% are parallel to the surface ( $\delta=90^\circ$ ). The second model, S2, assumes 8% OH groups with  $\delta=77^\circ$ , 51% with  $\delta=52^\circ$ , and the remaining 41% having  $\delta=15^\circ$ . The in plane orientation of the OH groups was randomly chosen at the start of every simulation and kept fixed subsequently.

### III. RESULTS FOR THE AIR/WATER INTERFACE

The air/water interface has been extensively studied by simulations for many years since the work of Wilson *et al.*,<sup>40-42</sup> and our simulations reported here reproduce those previous results. Our modeling of the air/water interface merely serves as the hydrophobic reference state, which is obtained for extrapolating to a contact angle of  $180^\circ$ .

#### A. Water orientation and surface potential

It is well known that water behaves quite differently than most known liquids. At the air/water interface, the most striking anomalies are the extraordinarily high surface tension ( $72 \text{ mN/m}$ ) (Ref. 9) and the observation of a surface potential.<sup>11</sup> The presence of a surface potential in the absence of charged particles (thus ignoring possible effects arising from the autoprotolysis of water) requires that water molecules at the border of the aqueous phase are oriented such that the charge distribution does not average to zero, and results in a nonvanishing polarization of the interface.

This is shown in Figs. 6 and 7. In Fig. 6 the mean of the cosine of the angle between the dipole moment and the sur-

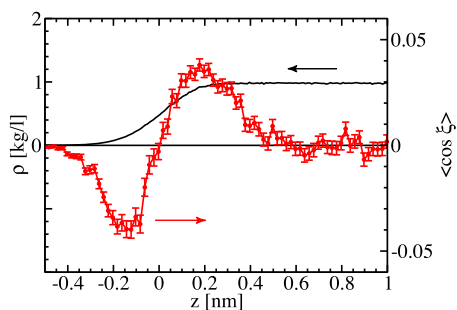


FIG. 6. Mean cosine of the angle  $\xi$  between the water dipole moment and the normal on the air/water interface (circles with error bars). A negative value of the cosine indicates that the dipole is pointing toward the vapor phase (i.e., H facing the vapor phase), a positive value indicates that it points to the water phase. Also shown for reference is the interfacial density profile (solid line). The surface potential at the air/water interface cannot be deduced from the orientational profile of the molecular dipole because the quadrupole moment of water cannot be neglected.

face normal is plotted. For reference, also the interfacial density profile is included in the graph. One can see that the mean cosine shows a fairly symmetrical profile around the center of the interface and then vanishes in the bulk liquid.

The overall drop in the electrostatic potential across the interface is about  $\Delta\phi = -600$  mV as can be seen in Fig. 7, which shows the profiles of the electrostatic potential and the mass density at the air/water interface. Our results for SPC/E water are in line with several other studies.<sup>12</sup> The consequences of these properties of the interface are dramatic. It is believed that ion adsorption at the air/water interface is induced by the properties of the interfacial water layers. This has recently been reviewed by Jungwirth and Tobias<sup>83</sup> and by Chang and Dang<sup>84</sup> along with many other implications.

The electrostatic potential profile cannot simply be deduced from the mean of the molecular dipole orientation because water molecules also carry a quadrupole moment, which is not specified by the dipole vector alone. In fact, the neglect of the quadrupole term results in a surface potential where even the sign is wrong.<sup>42</sup> The orientation of the water molecules and thus their quadrupole moment are exactly determined by the knowledge of the orientation of the molecular dipole vector and the orientation of the OH bond vectors. We further characterize the orientation of the interfacial wa-

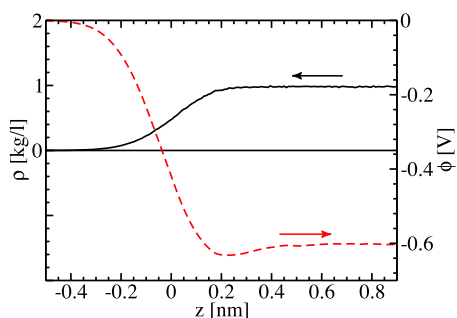


FIG. 7. Electrostatic potential (dashed line) and mass density (solid line) of pure water at the air/water interface as a function of the distance from the Gibbs dividing surface. The potential in the vapor phase is set to zero. The lateral size of the system is  $3.0 \times 3.0$  nm<sup>2</sup>.

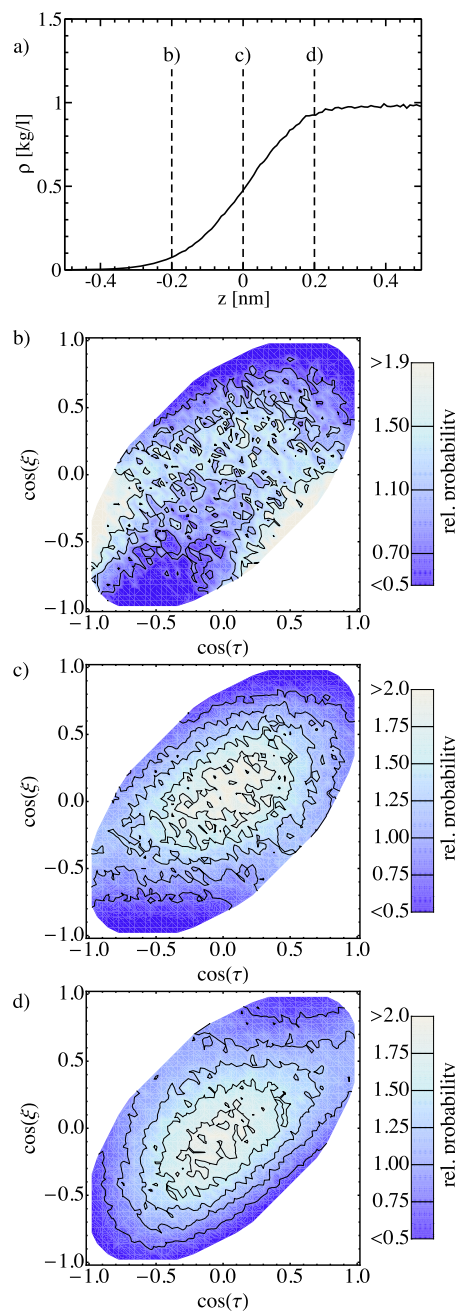


FIG. 8. (a) Mass density profile of the air/water interface. The dashed lines indicate the positions where the orientational distributions are calculated. [(b)–(d)] Joint probability distributions of  $\cos(\xi)$  and  $\cos(\tau)$  for different distances from the air/water interface, where  $\xi$  is the angle between the water dipole moment and the surface normal and  $\tau$  is the angle between the water OH vector and the surface normal. The scale for the color coding is shown besides the contour plots. The thickness of the vertical slices is  $2 \text{ \AA}$ .

ter molecules by the joint probability function of the angle between the water dipole moment and the surface normal,  $\xi$  and the angle between the water OH bond vectors and the surface normal,  $\tau$ . The normal vector is chosen such that it points toward the water phase.

Figures 8(b)–8(d) show the joint probability distributions of  $\cos(\xi)$  and  $\cos(\tau)$  for three vertical slices of  $2 \text{ \AA}$  thickness at different distances from the interface. The position of the

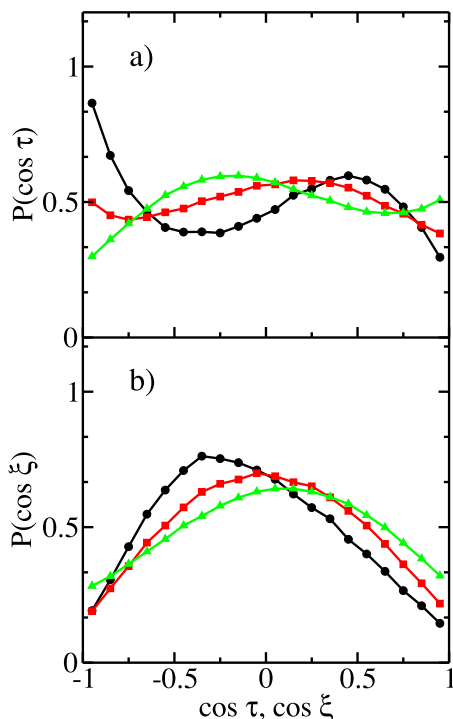


FIG. 9. (a) Probability distribution of the cosine of the angle between the water OH vector and the air/water interface normal. (b) Probability distribution of the cosine of the angle between the water dipole vector and the air/water interface normal. Circles corresponds to the leftmost slice, squares to the middle slice, and triangles to the rightmost slice in Fig. 8(a).

center of each slice is indicated by the dashed lines in the density profile Fig. 8(a). The corresponding one-dimensional distributions as a function of  $\cos(\xi)$  and  $\cos(\tau)$  for the same slices are shown in Fig. 9. In Fig. 9 the circles correspond to the  $z=-0.2$  nm slice, the squares to the  $z=0$  slice, and the triangles to the  $z=0.2$  nm slice marked in the density profile [Fig. 8(a)].

In all three layers, strong preferential orientation of the water molecules is observed. In the slice at  $z=-0.2$  nm [Fig. 8(b)], we see two strong maxima around  $(\cos \xi, \cos \tau) = (-0.5, -1.0)$  and  $(\cos \xi, \cos \tau) = (-0.5, 0.3)$ . These correspond to the same water molecule, where one of its H atoms is pointing directly toward the air, and consequently the other H atom is forming an angle of  $\approx 70^\circ$  with the normal (orientation I in Fig. 1). There is also a slightly smeared out peak around  $(\cos \xi, \cos \tau) = (0.3, 0.2)$ , which corresponds to a water molecule where both H atoms have the same  $z$ -coordinate, and the two OH bonds are slightly tilted toward the water phase (orientation IV in Fig. 1). In the following slice at  $z=0$  [Fig. 8(c)], the strong double peak is not present and the second maximum is increased in magnitude and shifted toward the origin. In this slice, the preferential orientation of the water molecules is parallel to the interface (orientation III in Fig. 1). In the slice at  $z=0.2$  nm [Fig. 8(d)], the situation is the opposite of that in the slice at  $z=-0.2$  nm (orientations II and V in Fig. 1). The maximum in the center is shifted to slightly negative  $\cos(\xi)$  and  $\cos(\tau)$ , and there is also evidence for water molecules with one hy-

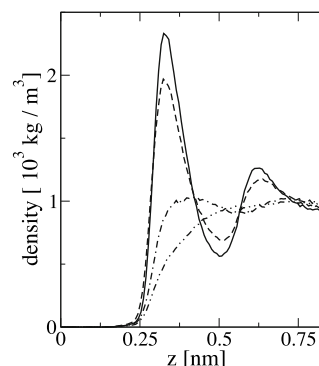


FIG. 10. Density profiles at the diamond/water interface. The diamond surface is located at  $z=0$ . With decreasing water-carbon interaction energy  $\epsilon_{LS}$ , the water density in the first peak at the interface decreases. The plot shows the profiles for interaction energies  $\epsilon_{LS}=0.72, 0.42, 0.18, 0.11$  kJ/mol.

drogen atom pointing toward the water phase, however with rather little probability. The same pattern can be observed in the one-dimensional probability distributions (Fig. 9). We finally note that the air/water interface is broadened by capillary waves.<sup>85</sup> Therefore, the distributions, which are calculated in slices that are defined with respect to the laboratory frame and do not account for the fluctuating nature of the interface, are to some extent washed out. The root mean square width of the interface in this study is 1.4 Å.

#### IV. RESULTS FOR NONPOLAR SURFACES

At a nonpolar solid/water interface, the situation is more complex than at the air/water interface because there are interactions between the water molecules and the wall atoms via Lennard-Jones potentials. The attractive interaction with the surface partly compensates for the loss of interaction partners of the water molecules near the surface. Furthermore, excluded volume effects lead to packing effects in the layers closest to the substrate and suppress capillary waves. Nevertheless, the qualitative behavior of water near nonpolar substrates is very similar to that at the air/water interface. In this section, a detailed comparison of different characteristic effects at both types of interfaces is presented.

##### A. Density profiles

In the bulk phase, we obtain densities around 0.98 kg/l for water. Density profiles of SPC/E water at diamond surfaces with different liquid-surface interactions  $\epsilon_{LS}$  (in the present case  $\epsilon_{LS}=\epsilon_{CO}$ ) are shown in Fig. 10. For the standard  $\epsilon_{CO}$  in the GROMOS96 force field, interfacial layering is visible in the first two water layers (dashed line in Fig. 10) where the density in the first water layer is increased by a factor of roughly two, compared to the bulk density. This layering effect becomes less pronounced with decreasing interaction strength  $\epsilon_{CO}$  and is totally absent for the lowest interaction energy. At the lowest interaction energy,  $\epsilon_{LS}=0.11$  kJ/mol, there is no layering, and the density profile has the form of the density profile at a liquid/air interface. Thus, by a continuous variation in  $\epsilon_{LS}$  we get a smooth transition from an air/water interface to a solid/water interface.

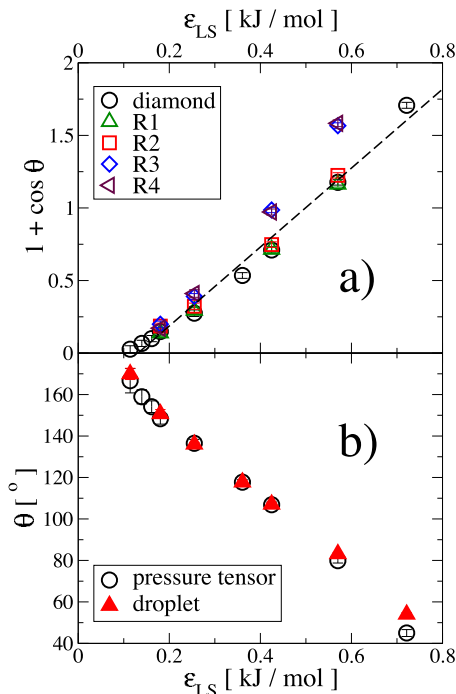


FIG. 11. (a) Contact angle obtained by the pressure tensor method for the diamond and R1, R2, R3, and R4 surfaces dependent on the solid/liquid interaction energy  $\varepsilon_{LS}$ . The dashed line is a linear fit for the simulation data of the smooth diamond. (b) Contact angle for the diamond obtained by the pressure tensor method (circles) and the droplet deposition method (triangles) dependent on the solid/liquid interaction energy  $\varepsilon_{LS}$ .

## B. Contact angles

The hydrophobicity of a surface is characterized by its contact angle  $\theta$  (Fig. 2). We calculate the contact angle of water at the interface to hydrophobic diamond for different  $\varepsilon_{LS}$  (0.72, 0.57, 0.42, 0.36, 0.25, 0.18, 0.16, 0.14, and 0.11 kJ/mol) as well as for different roughnesses following Eq. (6). In Fig. 11(a), we plot the results as  $1 + \cos(\theta)$  versus  $\varepsilon_{LS}$ . We obtain a nearly linear dependence of  $1 + \cos(\theta)$  as a function of  $\varepsilon_{LS}$ . This observation can be rationalized as follows: the surface tension of the solid/liquid interface can be calculated from the work  $H_{12}$  per surface area which is necessary to separate a slab of liquid from a slab of solid. This work is given as the sum of the surface energies of the two created interfaces, i.e., solid/vapor and liquid/vapor, minus the energy of the destroyed solid/liquid interface,

$$H_{12} = \gamma_{SV} + \gamma_{LV} - \gamma_{LS}. \quad (14)$$

The work  $H_{12}$  is calculated approximately, assuming homogeneous solid and liquid densities  $\rho_S$  and  $\rho_L$ ,  $H_{12} = -\pi\rho_S\rho_L\int_0^\infty r^3 V_{LS}(r)dr$ ,<sup>85</sup> with the intermolecular potential between liquid and solid,  $V_{LS}$ . For the Lennard-Jones potential,  $H_{12}$  is a linear function of  $\varepsilon_{LS}$ . From Young's equation it follows that the cosine of the contact angle is linearly dependent on the interaction energy,

$$1 + \cos \theta = \frac{\gamma_{SV} + \gamma_{LV} - \gamma_{LS}}{\gamma_{LV}} = \frac{H_{12}}{\gamma_{LV}} \propto \varepsilon_{LS}. \quad (15)$$

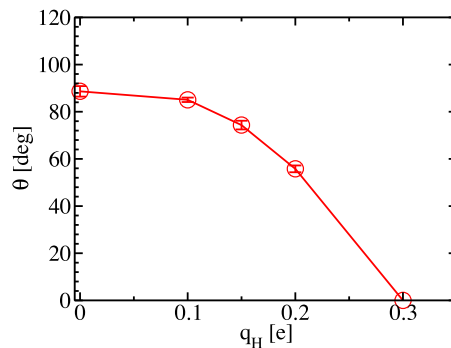


FIG. 12. Contact angle  $\theta$  for the hydrogen-terminated diamond with  $\varepsilon_{LS} = 0.54$  kJ/mol in dependence of the partial charge  $q_H$  of the hydrogen atoms. The contact angles are determined by the drop deposition method. For partial charges larger than  $0.3e$  the drop spreads out completely, thus the contact angle is 0. The line is just a guide to the eye.

As can be seen in Fig. 11(a), the linear dependence of  $1 + \cos \theta$  is a good fit to the data points. For smaller values of  $\varepsilon_{LS}$ , the depletion thickness increases and entropic effects connected to interfacial shape and density fluctuations become important, invalidating the simple arguments that lead to Eq. (15). In principle, one would expect complete drying, i.e.,  $\theta \rightarrow 180^\circ$ , as  $\varepsilon_{LS} \rightarrow 0$ . In Fig. 11(b) we replot the data as  $\theta$  versus  $\varepsilon_{LS}$ , which is more compatible with a drying transition as  $\varepsilon_{LS} \rightarrow 0$ . We also include data from droplet simulations that demonstrate excellent agreement between the two sets of data. We note that the contact angle  $\theta$  shows a non-trivial dependence on the cut off radius  $r_c$  used in simulations for the Lennard-Jones interaction. In comparison with experiments it is thus important to match experimental and simulated contact angles, since the surface interaction  $\varepsilon_{LS}$  alone does not fix the contact angle unambiguously.

One simplification used in nearly all studies of hydrophobic surfaces is that CH bonds are treated completely unpolarized. Their polarization is indeed small because the electronegativities of C and H are similar but there is still some polarization left, which is best described by a partial charge of the order of  $0.1e$  on the hydrogen atom. We test the validity of the neglect of CH polarization on the contact angle of water at the interface to hydrogen-terminated diamond. For this purpose we assign partial charges of  $q_H = 0.1, 0.15, 0.2,$  and  $0.3 e$  to the terminal hydrogen atoms and equal negative charges to the corresponding carbon atoms. The contact angle is determined by the drop deposition method for carbon-water interaction strength of  $\varepsilon_{LS} = 0.54$  kJ/mol. In Fig. 12 the contact angle is plotted versus the partial charge  $q_H$ . For partial charges smaller than  $0.15e$ , the contact angle changes only slightly, whereas for partial charges larger than  $0.2e$  a strong influence is seen. For partial charges greater than  $0.3 e$ , the drop spreads out completely on the surface, corresponding to a contact angle of  $\theta = 0$ . Realistic values for the partial charges of CH groups<sup>86,87</sup> lie well below the critical value where the influence on the contact angle becomes significant. Therefore, the neglect of polarization of the CH bonds is well grounded. If the simulation method was exact, one could deduce the polarization of the CH groups from the

dependence of the contact angle on the partial charges. However, the accuracy of the simulation approach (neglect of line tension, proper choice of  $\epsilon_{LS}$ , etc.) is not good enough to draw conclusion from the rather weak dependence for small  $q_H$ .

### C. Water orientation

In this paragraph, we show that the similarities of the air/water and the solid hydrophobic/water interface extend also to the orientations observed. Figures 13 and 14 show the orientation of the water molecules in the vicinity of a nonpolar diamond surface modeled with a carbon-water interaction strength of  $\epsilon_{LS}=0.54$  kJ/mol. The preferential orientations are similar to those for the air/water interface, but more distinctive since capillary waves are absent (note the different scale in the contour plots in Figs. 8 and 13). In the layer closest to the surface at  $z=0.25$  nm [Fig. 13(b)], there are again two predominant configurations. One corresponds to the double peak at  $(\cos \xi, \cos \tau)=(-0.5, -1.0)$  and  $(\cos \xi, \cos \tau)=(-0.5, 0.3)$  and represents a water molecule with one OH bond pointing toward the diamond surface (orientation I in Fig. 1). The other, dominant peak around  $(\cos \xi, \cos \tau)=(0.1, 0.1)$  corresponds to a water molecule almost parallel to the surface, but with the hydrogens slightly tilted to the bulk water phase (orientation IV in Fig. 1). In the following slice at  $z=0.29$  nm [Fig. 13(c)], which is located at the first peak in the density profile, the most probable orientation  $[(\cos \xi, \cos \tau)=(0.0, 0.0)]$  of the water molecules is parallel to the surface (orientation III in Fig. 1) and in the third slice at  $z=0.35$  nm [Fig. 13(d)] we observe again that the orientations are just the reverse of the orientations in the slice around  $z=0.25$  nm: there is a double peak at  $(\cos \xi, \cos \tau)=(0.5, 1.0)$  and  $(\cos \xi, \cos \tau)=(0.5, -0.3)$  and single peak at  $(\cos \xi, \cos \tau)=(-0.3, -0.2)$ . This corresponds to the orientations II and V in Fig. 1. A similar, albeit less pronounced pattern is observed at the second maximum in the density profile (not shown). This second peak is located at a distance of about 3 Å from the first peak, which is roughly the distance between the oxygen atoms of two hydrogen bonded water molecules. In the intermediate density minimum there is a smooth crossover between the orientations at the maxima. For larger separations from the surface no preferential orientations can be recognized any more.

Similar results for the water orientation at nonpolar surfaces have been found by previous studies of water at a structureless Lennard-Jones wall<sup>43</sup> and at idealized self-assembled monolayers.<sup>30</sup> Lee *et al.*<sup>43</sup> have explained these by a dominating structure that is similar to the crystal structure of ice I, with the *c*-axis perpendicular to the hydrophobic surface (see Fig. 9 in Ref. 43). Such a structure balances the competition between packing forces that tend to produce a dense layer in contact with the surface and the tendency of the water molecules to maintain as many hydrogen bonds as possible. It allows the water molecules to form an almost planar layer at the expense of only one hydrogen bond that is broken for those molecules closest to the surface. The predominant orientations of the water molecules in the layers

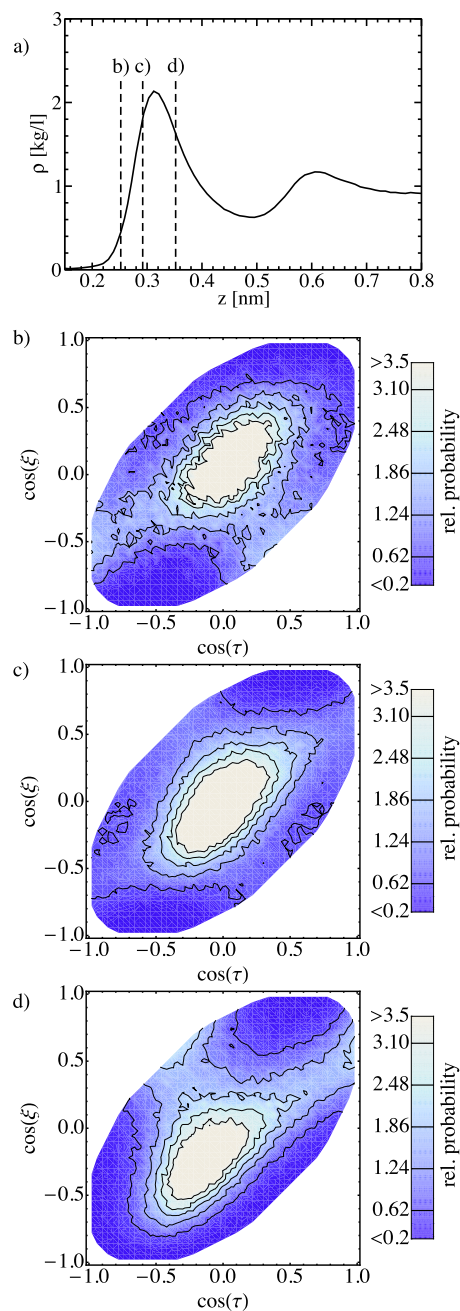


FIG. 13. Density profile and orientational distributions at a nonpolar surface with  $\epsilon_{LS}=0.54$  kJ/mol. (a) Mass density profile. The dashed lines indicate the positions where the orientational distributions are calculated. [(b)–(d)] Joint probability distributions of  $\cos(\xi)$  and  $\cos(\tau)$  for different distances from the surface, where  $\xi$  is the angle between the water dipole moment and the surface normal and  $\tau$  is the angle between the water OH vector and the surface normal. The scale for the color coding is shown besides the contour plots. The thickness of the layers considered is 0.2 Å.

adjacent to the surface associated with this view are consistent with those observed in our study. However, it is misleading to relate the observation of ordered structures with an overall decrease in entropy because there are translational and orientational effects that contribute to the entropy. The surface tension of water becomes smaller with increasing temperature,<sup>88</sup> which implies that the excess entropy of water at the interface is positive. This decrease in the surface ten-

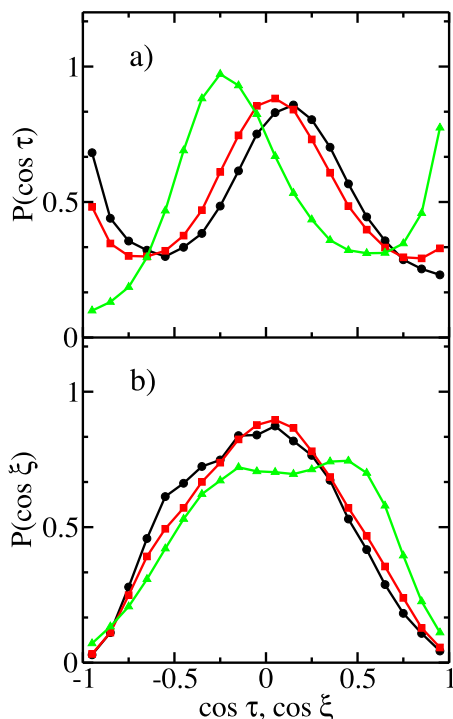


FIG. 14. Orientation of water at a nonpolar surface with  $\epsilon_{LS}=0.54$  kJ/mol. (a) Probability distribution of the cosine of the angle between the water OH vector and the surface normal. (b) Probability distribution of the cosine of the angle between the water dipole vector and the surface normal. Circles corresponds to the leftmost slice, squares to the middle slice, and triangles to the rightmost slice in Fig. 13(a).

sion with temperature at an extended interface is in remarkable contrast to the hydrophobic solvation of small particles such as methane molecules or rare gas atoms for which the solvation entropies are negative.<sup>89</sup> This shows the nontrivial dependence of the hydrophobic effect on the solute size.<sup>8</sup>

Similar to the air/water interface, the orientation of the water molecules at the solid hydrophobic/water interface induces an average polarization of the interface. The mean orientation of the water dipole moment and the electrostatic potential are shown in Figs. 15 and 16. We see an oscillatory

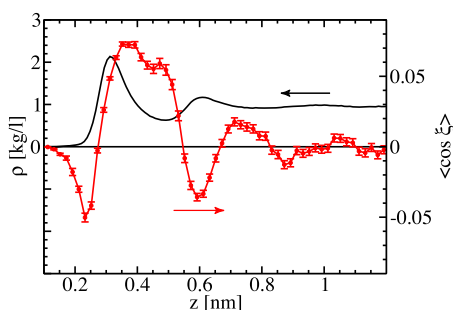


FIG. 15. Mean cosine (circles with error bars) of the angle  $\xi$  between the water dipole moment and the normal at a nonpolar surface with  $\epsilon_{LS}=0.54$  kJ/mol. A negative value of the cosine means that the dipole of the water molecule is pointing toward the surface, i.e., the H-atoms are facing the surface. A positive value means that the dipole moment points toward the water phase. Also shown for reference is the interfacial density profile (solid line).

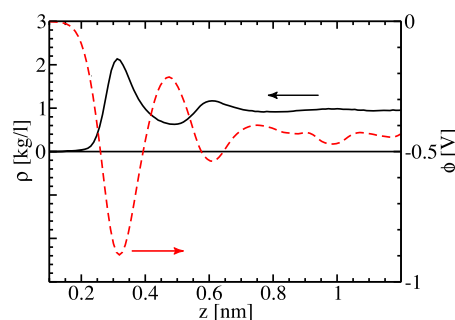


FIG. 16. Electrostatic potential (dashed line) as a function of the distance from a nonpolar surface with  $\epsilon_{LS}=0.54$  kJ/mol. The potential in the substrate is set to zero. Also shown for reference is the interfacial density profile (solid line).

behavior of  $\langle \cos \xi \rangle$  as a function of  $z$  similar to that at the air/water interface but reaching further into the liquid phase. The overall potential drop ( $\Delta\phi \approx -450$  mV) is however comparable to that at the air/water interface, and many effects that occur at the air/water interface are likely to be seen also at the solid hydrophobic/water interface. Especially, the electric field present at a hydrophobic surface is capable of attracting large anions such as iodide<sup>90,91</sup> similar to the air/water interface.<sup>83</sup>

#### D. Shear flow

Here, we study the effects of hydrophobicity on hydrodynamic flows, which are described by the Navier–Stokes equation with appropriate boundary conditions. Over the past years it has become clear that for hydrophobic surfaces the no-slip boundary condition (i.e., zero interfacial fluid velocity) does not necessarily hold at nanoscopic length scales.<sup>92,93</sup> At hydrophobic surfaces, partial slip occurs which can be described by a slip length  $b$ , defined in Eq. (10) and the gradient of the fluid velocity field in parallel direction to the surface normal at the position of the surface. Although experimentally observed slip lengths of nanometers up to micrometers have been reported,<sup>92</sup> there is growing evidence for slip lengths in the nanometer range, for example, 20 nm at a surface with contact angle  $\theta=105^\circ$ .<sup>33</sup> This is still larger than the predicted slip length from MD. In our simulations we demonstrate that the slip length is independent of the shear rate (see Fig. 17), which excludes the difference in shear rates as the reason for the difference between experiment and MD. A possible explanation is the presence of adsorbed gas at the interface.

We investigate how the slip length at the diamond/water interface depends on the surface properties and simulation parameters.

##### 1. Shear rate and water film thickness

For the study of the influence of the shear rate and the water slab thickness on the slip length, several simulations are performed, where we vary these parameters systematically. The results are summarized in Fig. 17 where the thickness of the water slab was varied from 2 up to 8 nm with

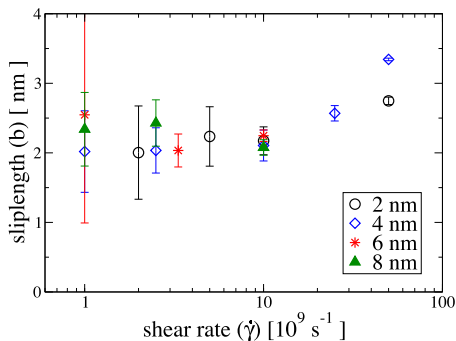


FIG. 17. Slip length vs shear rate for water film thicknesses of  $Z=2, 4, 6,$  and  $8$  nm with an interaction energy  $\epsilon_{LS}=0.42$  kJ/mol.

shear rates ranging from  $10^9$  up to  $5 \times 10^{10} \text{ s}^{-1}$  for a fixed interaction parameter  $\epsilon_{LS}=0.42$  kJ/mol. A slip length of the order of 2 nm is obtained in all simulations, which shows that the slip length  $b$  is insensitive to the water film thickness and demonstrates that bulklike behavior for the water film is obtained even for the thinnest films. Up to shear rates of  $10^{10} \text{ s}^{-1}$ ,  $b$  is almost independent on the shear rate. Therefore the shear rate  $\dot{\gamma}=10^{10} \text{ s}^{-1}$  used for the simulations in the following section is appropriate to obtain reasonable results.

**2. Surface properties**

We further analyze the influence of the surface properties on the slip. For that purpose, we focus on the slip length at smooth and rough surfaces and its change with the interaction energy  $\epsilon_{LS}$ . It is known that especially the wettability of the surface has a strong influence on the obtained slip length.<sup>93</sup>

Figure 18 shows the slip length for different surfaces, dependent on the interaction energy  $\epsilon_{LS}$ . As can be seen clearly, for the rough surfaces, the slip length is substantially lower than at the smooth diamond surface. This is due to the fact that increasing roughness leads to increased friction at the solid/liquid interface and therefore diminishes the slip. As can be seen in Fig. 18, the slip length is proportional to the inverse square of the interaction energy.

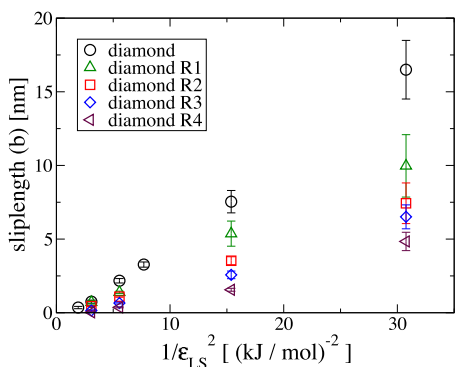


FIG. 18. Slip length at different surfaces with varying interaction energy  $\epsilon_{LS}$ , all obtained for constant water film thickness of 4 nm and shear rate  $\dot{\gamma}=10^{10} \text{ s}^{-1}$ .

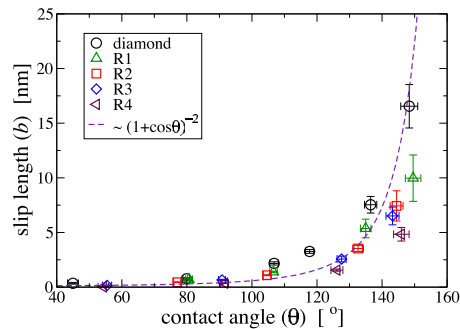


FIG. 19. Slip length vs contact angle for all considered surfaces and interaction parameters, with constant water film thickness of 4 nm and shear rate  $\dot{\gamma}=10^{10} \text{ s}^{-1}$ .

In Ref. 35 a Kubo relation for the friction force, exerted by the wall on the fluid is derived and set in relation to the amount of slip. From that calculation one can infer that  $b \propto \epsilon_{LS}^{-2}$ .<sup>77</sup> This relation is confirmed by the simulation data shown in Fig. 18. Noting that  $\cos \theta_c + 1 \propto \epsilon_{LS}$ , as shown in Fig. 11(a), a quite universal relation between the amount of slippage and the contact angle can be given,  $b \propto (1 + \cos \theta)^{-2}$ .<sup>77</sup> Astonishingly, this relation turns out to be quite universal in terms of surface structure since the simulation data collapse approximately on one single curve (see Fig. 19). Even for very hydrophobic surfaces with contact angles of  $150^\circ$ , the slip does not exceed 20 nm.

**3. Influence of the depletion length**

Another theory<sup>24</sup> for the slip length at the liquid/solid interface relates the presence of a depletion layer of thickness  $\delta$  with a viscosity  $\eta_G$  that is substantially lower than the bulk water viscosity  $\eta_L$ . Following this idea and assuming the viscosity  $\eta_G$  not to depend on the depletion layer width, an expression for the slip length is obtained, which is linearly dependent on the width of the depletion layer,  $b = \delta(\eta_L / \eta_G - 1)$ .<sup>24</sup> We compare our results with this theory using two different definitions of the vapor layer width  $\delta$ : (i) first, we use the distance between the topmost surface layer and the position where the water density first reaches half its bulk value. This is the definition applied in Ref. 24. (ii) Alternatively, we use the depletion length  $\delta = d_1$  as defined in Eq. (2). Using both definitions, we do not observe a linear dependence of the slip length on the depletion layer width. This can be seen in Fig. 20. Therefore, the simple picture of two viscosities, where the viscosity is constant throughout the depletion layer, cannot hold as an explanation for the observed slip at a hydrophobic surface.

**V. RESULTS FOR WATER AT POLAR SUBSTRATES**

The requirement that hydrophobic surfaces contain ideally no polar surface groups puts a tight constraint on the multitude of possible chemical compositions of such a surface. This constraint does not hold for polar surfaces, and there is an extreme variety of different surface compositions. Simple and intuitive descriptions of hydrophilic substrates are constituted by atomistic models of the solid phase that account

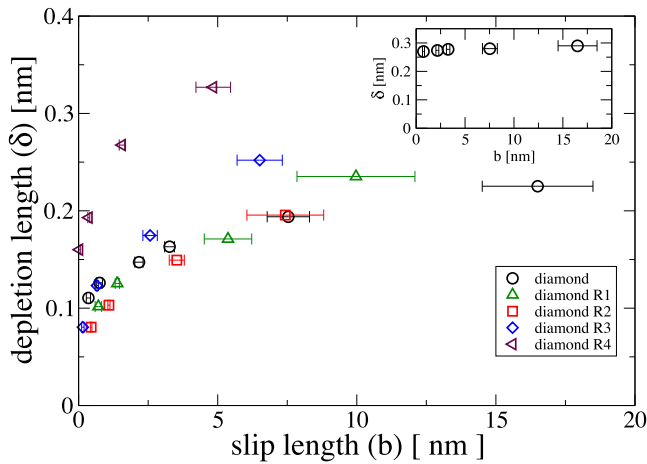


FIG. 20. Depletion length  $\delta$  vs the slip length  $b$ . In the main figure, the depletion length  $\delta$  was determined using Eq. (2). In the inset, the criterion from Ref. 24, where  $\delta$  is defined as the distance from the surface where the water density reaches half its bulk value, was used.

for the specific nature of the surface and the interactions with water molecules arising from them. One example is the model of graphite-water interactions<sup>19,73</sup> that considers specific interactions between the water’s hydrogen and carbon atoms. Another example is a polar surface with functional groups such as OH and COOH. The main issue in studying

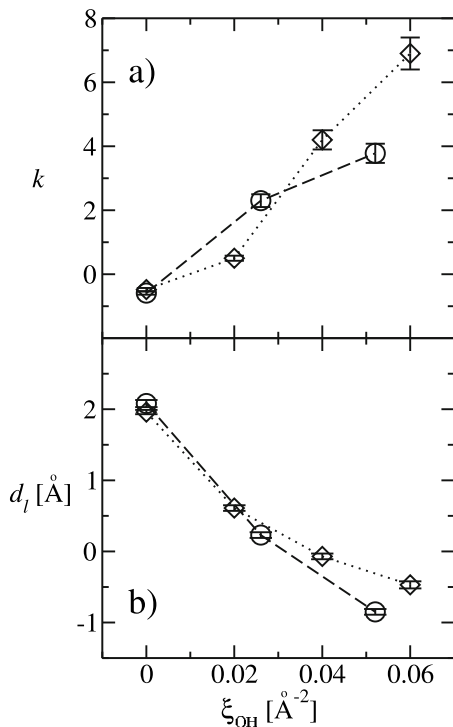


FIG. 21. Wetting coefficient  $k$  and the depletion thickness  $d_l$  as a function of the surface density  $\xi_{OH}$  of hydroxyl groups for tetragonal (circles) and hexagonal (diamonds) arrangement of the solid surface. The hydroxyl groups are distributed regularly on the surface, the rotation of OH groups is frozen, and the inclination of OH bonds from the normal direction is always  $\delta = 71.5^\circ$ .

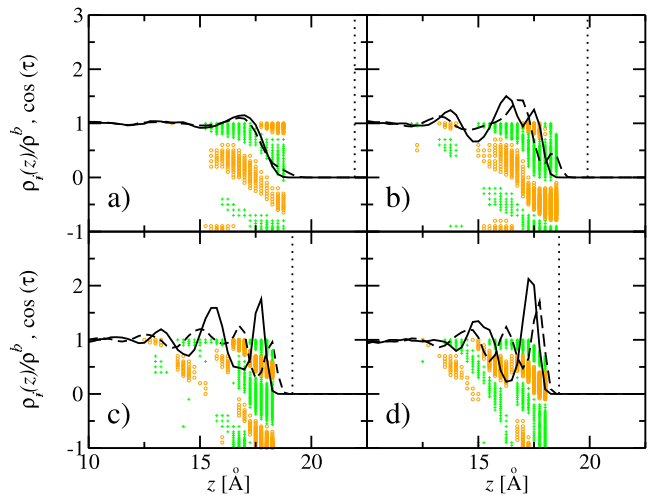


FIG. 22. Density profiles of the oxygen (solid lines) and hydrogen (dashed lines) sites of water in contact with a hexagonal solid lattice with different fraction of OH groups: (a)  $x_{OH}=0$ , (b)  $x_{OH}=1/3$ , (c)  $x_{OH}=2/3$ , and (d)  $x_{OH}=1$ . The circles denote values of the cosine of the angle between water-OH bonds and the water-surface normal which occur with probability larger than 0.6; crosses denote orientations that occur with probability less than 0.4. Distances for which neither circles nor crosses are plotted are characterized by rather isotropic orientational distributions. The vertical dotted lines show the positions of the first layers of sites of the solid phase. The OH groups are distributed regularly and their orientation is kept fixed, the inclination angle is  $\delta=71.5^\circ$ .

such surfaces is the huge amount of possible variations of spatial distribution, orientation, flexibility, etc. of these polar groups.

Recently, a set of idealized models of solid phases was studied in order to separate the effects of particular parameters which characterize a polar substrate, such as the density of hydrophilic groups, their distribution, flexibility and orientation.<sup>30</sup> In the first part, the effect of increasing surface density of OH groups was studied using regularly distributed hydroxyl groups with fixed inclination angle  $\delta=71.5^\circ$  and all the OH bonds parallel. Two types of site arrangements, tetragonal and hexagonal, were studied. The obtained values of the wetting coefficient and depletion thickness are plotted in Fig. 21 as a function of the surface density of hydroxyl groups,  $\xi_{OH}$ . An increase in the density of the OH groups increases the wetting coefficient, and more water molecules come closer to the surface, which results in a decreased density reduction in the interfacial region. The difference in the structure of the surface between tetragonal and hexagonal lattice causes subtle differences.

The course of density profiles of the oxygen (solid line) and hydrogen (dashed line) atoms of water are shown for different surface fractions of OH bonds in Fig. 22 for systems with hexagonal arrangement. The four parts of the diagram correspond to increasing fractions of OH groups in the surface layer from  $x_{OH}=0$  [part (a)-hydrophobic substrate] to  $x_{OH}=1/3$  (b),  $x_{OH}=2/3$  (c) to  $x_{OH}=1$  (d). The gradual transformation of the flat maximum on the oxygen site density profile to sharper and higher peak is caused by specific interactions between the polar surface groups and the water molecules. For  $x_{OH}=2/3$  and  $x_{OH}=1$ , two distinct peaks are

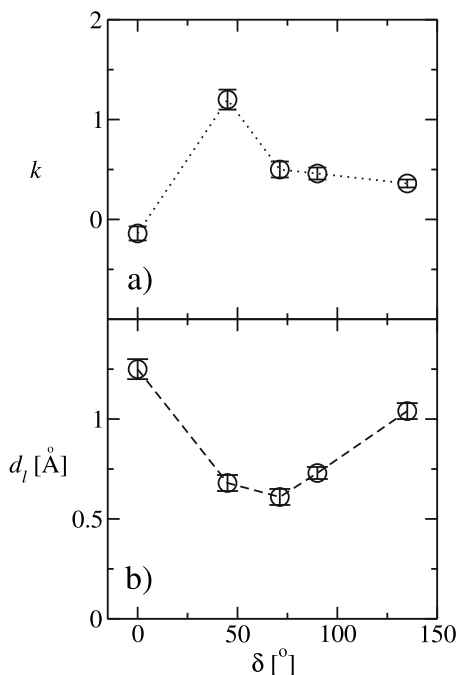


FIG. 23. (a) Wetting coefficient  $k$  and (b) depletion thickness  $d_l$  as a function of the inclination angle  $\delta$  between the surface OH bonds and the surface normal, which point toward the water phase. The considered solid substrate has hexagonal geometry, is completely rigid, and the hydroxyl groups are distributed regularly on the surface. The surface fraction of OH groups is  $x_{\text{OH}}=1/3$ .

observed, which can be interpreted as the existence of two adsorbed water layers. The high increase in the wetting coefficient between  $x_{\text{OH}}=1/3$  and  $x_{\text{OH}}=2/3$  in Fig. 21(a) is interpreted by synergistic effects of neighboring OH groups: in the case  $x_{\text{OH}}=1/3$ , these groups are isolated and thus each water molecule can interact with one hydroxyl group only, but for higher coverage there is a possibility that water molecules assume a “bridging” geometry with two hydrogen bonds to neighboring surface groups. The dotted vertical lines in Fig. 22 indicate the positions of the oxygen atoms of the surface-attached hydroxyl groups. In the case of substrates with tetragonal arrangement of sites the situation is further complicated by the fact that the water molecules can penetrate between the sites in the first layer of the solid substrate, as explained in Ref. 30.

For the hexagonal lattice with  $x_{\text{OH}}=1/3$  (regularly distributed and with fixed orientation of the OH bonds in the  $xy$ -plane), the influence of the inclination angle  $\delta$ , was also studied. The values of the wetting coefficient and the thickness of the depletion layer are plotted in Fig. 23 as a function of the inclination angle  $\delta$ . It is evident that the hydrophilicity reaches a maximum around  $\delta=45^\circ$ . This is explained by the capability of OH groups with various inclinations to form hydrogen bonds with water molecules. In the optimal orientation  $\delta=45^\circ$  two water molecules can be bonded to an OH group through their hydrogen atoms and a third one can serve as a donor of an electron pair and bond to the hydrogen atom of the hydroxyl group. For  $\delta=0^\circ$  the positive partial charge of the hydrogen atom shields the oxygen, which thus

cannot bind any water hydrogens. Thus, at most one hydrogen bond per hydroxyl group can be formed. Moreover, the water molecules in the surface layer are preferentially oriented with one OH bond pointing toward the substrate, which leads to strong dipole-dipole repulsion. If the bond angle of the surface OH groups is slightly increased, the hydrogen atom of the OH group is still reaching out into the water phase and is ready to serve as an acceptor for the electron pair of a water molecule, but at the same time the OH oxygen atom is reachable by water hydrogen atoms. As the inclination angle  $\delta$  becomes larger than  $90^\circ$ , the hydrogen of the hydroxyl group is hidden by the larger oxygen atom and is not available for hydrogen bond formation, which lowers the hydrophilicity of the surface. Nevertheless, since the surface oxygen can bind more than one water molecule, the surface with  $\delta \geq 90^\circ$  remains fairly hydrophilic.<sup>30</sup> This intricate dependence of the capability to form hydrogen bonds of surface hydroxyl groups on their angle of orientation was recently confirmed experimentally by sum-frequency generation experiments on sapphire surfaces.<sup>82</sup> On these surfaces a pH-dependent distribution of OH groups of various orientations is present, and the affinity to bind water of groups with different orientations can be analyzed and was found to roughly agree with the picture derived from simulations.

These experiments prompted a more realistic modeling of the different angular distributions of OH groups on sapphire surfaces. For the two models S1 and S2 three lattices were constructed with different orientations of the surface OH groups in the  $xy$ -plane. This variance influenced the wetting properties of the surfaces considerably. For model S1 (here 2/3 of the OH groups have an inclination angle  $\delta=90^\circ$ , the rest have  $\delta=0^\circ$ ) the wetting coefficient  $k$  is between  $-0.5$  and  $1.2$ , while for S2 (where 8% of the OH groups have an inclination angle  $\delta=77^\circ$ , 51% an angle  $\delta=52^\circ$  and the rest have  $\delta=15^\circ$ ) only values corresponding to superhydrophilic character are obtained (wetting coefficient  $k$  between  $1.5$  and  $2.9$ ). The difference follows from the lower ability of OH groups in the S1 model to form hydrogen bonds with interfacial water molecules (in agreement with our above discussed model simulations studying the influence of the inclination angle  $\delta$ ). The density profiles for these two models are shown in Fig. 24. One can see a pronounced adsorption peak where the density is three times higher than in the bulk phase. In this layer the water molecules are oriented preferably with one OH bond pointing outward from the water phase (the density of hydrogen atoms shows its first maximum about  $1 \text{ \AA}$  closer to the solid surface) which is favorable mostly for hydrogen bond formation to other water molecules in farther layers. The hydrogen bonds to surface OH groups of sapphire are possible only for groups with inclination angle  $\delta$  lower than  $\approx 75^\circ$ . Clearly the model S2 includes more such groups which explain the increased value of the wetting coefficient.

Another model of a solid substrate was employed in the simulations in Ref 26. A lattice of alkane chains partially terminated by OH groups was slightly tilted and free rotation

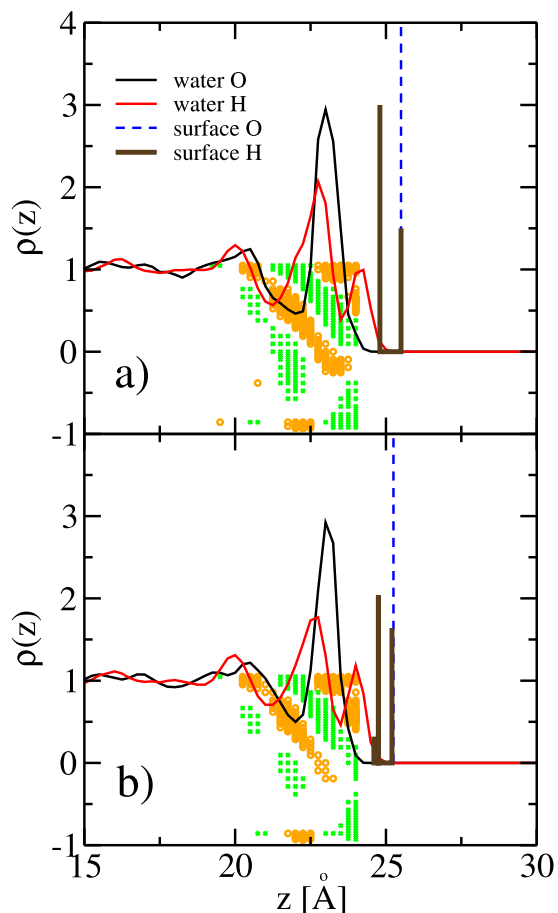


FIG. 24. Density profiles for water in contact with sapphire model S1 (part a) and S2 (part b). The positions of the surface oxygens and hydrogens are shown by full (H) and dashed (O) horizontal bars. The heights of the full bars correspond to the fraction of H atoms at the position of the bar. The black and gray curves are the densities of the water O and H atoms. The circles denote values of the cosine of the angle between water-OH bonds and the water surface normal which occur with probability larger than 0.6, the crosses denote orientations that occur with probability less than 0.4.

of the OH groups around the C–O bond was allowed. Thanks to the tilting of the alkane chains the angle between the OH bond and normal direction varied in a range of about  $30^\circ$ – $110^\circ$ . The relation between the thickness of the depletion layer and wetting coefficient was studied for different combinations of substrates and liquids (polar substrate–water, nonpolar substrate–water, polar substrate–organic liquid, nonpolar substrate–organic liquid). It was found that depletion not only occurs at the interface between a hydrophobic substrate and a polar (water) liquid, but also between a hydrophilic surface and nonpolar solvent. These simulation results were in agreement with corresponding neutron reflectivity experiments and suggest that depletion layers are more generally occurring between phases of mismatching polarity.<sup>26</sup>

## VI. SUMMARY AND OUTLOOK

We have reviewed some new results in the modeling of water at solid walls. Due to the rather high rigidity of the studied walls, disorder of the surface and fluctuations of the

interface caused by capillary waves are not important, in sharp contrast to the interfaces between water on one side and air, nonpolar liquids,<sup>94</sup> and membranes<sup>95</sup> on the other side. The interfacial water structure at such solid interfaces has long-reaching consequences for a large variety of phenomena. At hydrophobic solids, the general water behavior is very similar to the one at the air/water interface. The interactions between the solid and the water molecules are rather negligible, which give rise to slippage effects in hydrodynamic flows<sup>77</sup> and to large mobilities of single molecules.<sup>96</sup> The orientation of water in the interfacial layer gives rise to a strong interfacial electrostatic potential, with consequences on the adsorption of charged solutes. On hydrophobic surfaces, the only tunable parameter is the surface-water interaction strength. In our model surfaces we achieve this by a systematic variation of the Lennard-Jones parameters. In real systems, a change in interaction is typically brought about by a change in the density of the solid.

The behavior at hydrophilic surfaces is drastically different: there, the dominant factor governing the orientation of interfacial water molecules is the direct hydrogen bonding between water molecules and surface OH groups. In a lateral flow, the classic no-slip boundary condition determines hydrodynamic flows, and lateral motion of adsorbed molecules is limited by the breaking and reformation of short-ranged specific interactions like hydrogen bonds. The example of the sapphire surface nicely demonstrates that the specific properties of hydrophilic surfaces sensitively depend on the orientation and density of surface hydroxyl groups.

Besides surfaces with homogeneous wetting properties, there are also inhomogeneous surfaces, which are composed of hydrophobic and hydrophilic patches. The most prominent example is undoubtedly proteins, where the different behaviors of water at different patches of the surface cause the hydrophobic collapse during folding. Along the lines presented in this review, a thorough study of such surfaces has the prospect of gaining deeper insight into the properties of water close to such surfaces, but the inhomogeneity of the surface further increases the complexity of the systems to study.

The probably most important consequence of the peculiarities of interfacial water is its ability to induce attraction of solute molecules and ions. Adsorption of solutes at interfaces is driven by interplay of direct solute-surface interactions and solvation forces.<sup>97</sup> These solvation forces are intimately connected with the structure of water in the interfacial region, and are therefore determined by complex interactions in a high-dimensional space. As a consequence, attempts to analytically describe the solvation forces at interfaces are therefore difficult and have not been achieved in a predictive manner.<sup>90</sup>

<sup>1</sup>P. Ball, *Chem. Rev.* (Washington, D.C.) **108**, 74 (2008).

<sup>2</sup>E. W. Lang and H. D. Ludemann, *Angew. Chem., Int. Ed. Engl.* **21**, 135 (1982).

<sup>3</sup>G. Hummer, S. Garde, A. E. Garcia, M. E. Paulaitis, and L. R. Pratt, *J. Phys. Chem. B* **102**, 10469 (1998).

- <sup>4</sup>S. Garde, G. Hummer, A. E. Garcia, M. E. Paulaitis, and L. R. Pratt, *Phys. Rev. Lett.* **77**, 4966 (1996).
- <sup>5</sup>G. Hummer, S. Garde, A. E. Garcia, M. E. Paulaitis, and L. R. Pratt, *Proc. Natl. Acad. Sci. U.S.A.* **95**, 1552 (1998).
- <sup>6</sup>Y. Levy and J. N. Onuchic, *Annu. Rev. Biophys. Biomol. Struct.* **35**, 389 (2006).
- <sup>7</sup>G. Hummer, S. Garde, A. E. Garcia, A. Pohorille, and L. R. Pratt, *Proc. Natl. Acad. Sci. U.S.A.* **93**, 8951 (1996).
- <sup>8</sup>D. Chandler, *Nature (London)* **437**, 640 (2005).
- <sup>9</sup>N. L. Jarvis and M. A. Scheiman, *J. Phys. Chem.* **72**, 74 (1968).
- <sup>10</sup>P. Atkins, *Physical Chemistry* (Oxford University Press, New York, 1998).
- <sup>11</sup>M. Paluch, *Adv. Colloid Interface Sci.* **84**, 27 (2000).
- <sup>12</sup>V. P. Sokhan and D. J. Tildesley, *Mol. Phys.* **92**, 625 (1997).
- <sup>13</sup>P. G. de Gennes, *Rev. Mod. Phys.* **57**, 827 (1985).
- <sup>14</sup>J. N. Israelachvili, *Intermolecular and Surface Forces* (Academic, New York, 1991).
- <sup>15</sup>J. Genzer and K. Efimenko, *Science* **290**, 2130 (2000).
- <sup>16</sup>L. Feng *et al.*, *Adv. Mater. (Weinheim, Ger.)* **14**, 1857 (2002).
- <sup>17</sup>J. Love, L. Estroff, J. Kriebel, R. Nuzzo, and G. Whitesides, *Chem. Rev. (Washington, D.C.)* **105**, 1103 (2005).
- <sup>18</sup>F. Schreiber, *Prog. Surf. Sci.* **65**, 151 (2000).
- <sup>19</sup>T. Werder, J. H. Walther, R. L. Jaffe, T. Halicioglu, and P. Koumoutsakos, *J. Phys. Chem. B* **107**, 1345 (2003).
- <sup>20</sup>A. Härtl, J. A. Garrido, S. Nowy, R. Zimmermann, C. Werner, D. Horinek, R. R. Netz, and M. Stutzmann, *J. Am. Chem. Soc.* **129**, 1287 (2007).
- <sup>21</sup>X. Li, J. Li, M. Eleftheriou, and R. Zhou, *J. Am. Chem. Soc.* **128**, 12439 (2006).
- <sup>22</sup>R. Steitz, T. Gutberlet, T. Hauss, B. Klösgen, R. Krastev, S. Schemmel, A. C. Simonsen, and G. H. Findenegg, *Langmuir* **19**, 2409 (2003).
- <sup>23</sup>D. Schwendel, T. Hayashi, R. Dahint, A. Pertsin, M. Grunze, R. Steitz, and F. Schreiber, *Langmuir* **19**, 2284 (2003).
- <sup>24</sup>D. A. Doshi, E. B. Watkins, J. N. Israelachvili, and J. Majewski, *Proc. Natl. Acad. Sci. U.S.A.* **102**, 9458 (2005).
- <sup>25</sup>M. Mezger, H. Reichert, S. Schoder, J. Okasinski, H. Schröder, H. Dosch, D. Palms, J. Ralston, and V. Honkimaki, *Proc. Natl. Acad. Sci. U.S.A.* **103**, 18401 (2006).
- <sup>26</sup>M. Maccarini *et al.*, *Langmuir* **23**, 598 (2007).
- <sup>27</sup>K. Lum, D. Chandler, and J. Weeks, *J. Phys. Chem. B* **103**, 4570 (1999).
- <sup>28</sup>D. Huang and D. Chandler, *J. Phys. Chem. B* **106**, 2047 (2002).
- <sup>29</sup>S. I. Mamatkulov, P. K. Khabibullaev, and R. R. Netz, *Langmuir* **20**, 4756 (2004).
- <sup>30</sup>J. Janček and R. R. Netz, *Langmuir* **23**, 8417 (2007).
- <sup>31</sup>P. Koelsch *et al.*, *Colloids Surf., A* **303**, 110 (2007).
- <sup>32</sup>B. M. Ocko, A. Dhinojwala, and J. Daillant, *Phys. Rev. Lett.* **101**, 039601 (2008).
- <sup>33</sup>C. Cottin-Bizonne, B. Cross, A. Steinberger, and E. Charlaix, *Phys. Rev. Lett.* **94**, 056102 (2005).
- <sup>34</sup>O. I. Vinogradova and G. E. Yakubov, *Langmuir* **19**, 1227 (2003).
- <sup>35</sup>J.-L. Barrat and L. Bocquet, *Phys. Rev. Lett.* **82**, 4671 (1999).
- <sup>36</sup>J.-L. Barrat and L. Bocquet, *Faraday Discuss.* **112**, 119 (1999).
- <sup>37</sup>H. Stone, A. Stroock, and A. Ajdari, *Annu. Rev. Fluid Mech.* **36**, 381 (2004).
- <sup>38</sup>J. F. H. Stillinger and A. Ben-Naim, *J. Chem. Phys.* **47**, 4431 (1967).
- <sup>39</sup>C. A. Croxton, *Phys. Lett.* **74**, 325 (1979).
- <sup>40</sup>M. A. Wilson, A. Pohorille, and L. R. Pratt, *J. Phys. Chem.* **91**, 4873 (1987).
- <sup>41</sup>M. A. Wilson, A. Pohorille, and L. R. Pratt, *J. Chem. Phys.* **88**, 3281 (1988).
- <sup>42</sup>M. A. Wilson, A. Pohorille, and L. R. Pratt, *J. Chem. Phys.* **90**, 5211 (1989).
- <sup>43</sup>C. Y. Lee, J. A. McCammon, and P. J. Rossky, *J. Chem. Phys.* **80**, 4448 (1984).
- <sup>44</sup>S. H. Lee and P. J. Rossky, *J. Chem. Phys.* **100**, 3334 (1994).
- <sup>45</sup>A. Wallqvist, *Chem. Phys. Lett.* **165**, 437 (1990).
- <sup>46</sup>J. R. Grigera, S. G. Kalko, and J. Fischbarg, *Langmuir* **12**, 154 (1996).
- <sup>47</sup>T. Hayashi, A. J. Pertsin, and M. Grunze, *J. Chem. Phys.* **117**, 6271 (2002).
- <sup>48</sup>K. Raghavan, K. Foster, K. Motakabbir, and M. Berkowitz, *J. Chem. Phys.* **94**, 2110 (1991).
- <sup>49</sup>E. Spohr, *J. Phys. Chem.* **93**, 6171 (1989).
- <sup>50</sup>E. Spohr and K. Heinzinger, *Chem. Phys. Lett.* **123**, 218 (1986).
- <sup>51</sup>K. Heinzinger and E. Spohr, *Electrochim. Acta* **34**, 1849 (1989).
- <sup>52</sup>H. Shinto, T. Sakakibara, and K. Higashitani, *J. Phys. Chem. B* **102**, 1974 (1998).
- <sup>53</sup>H. Heller, M. Schaefer, and K. Schulten, *J. Phys. Chem.* **97**, 8343 (1993).
- <sup>54</sup>M. A. Wilson and A. Pohorille, *J. Am. Chem. Soc.* **116**, 1490 (1994).
- <sup>55</sup>O. Berger, O. Edholm, and F. Jahnig, *Biophys. J.* **72**, 2002 (1997).
- <sup>56</sup>S.-J. Marrink, O. Berger, P. Tieleman, and F. Jahnig, *Biophys. J.* **74**, 931 (1998).
- <sup>57</sup>A. Ismail, G. Grest, and M. Stevens, *Langmuir* **23**, 8508 (2007).
- <sup>58</sup>A. J. Pertsin, T. Hayashi, and M. Grunze, *J. Phys. Chem. B* **106**, 12274 (2002).
- <sup>59</sup>A. J. Pertsin and M. Grunze, *Langmuir* **16**, 8829 (2000).
- <sup>60</sup>A. Delville, *J. Phys. Chem.* **97**, 9703 (1993).
- <sup>61</sup>D. Frenkel and B. Smit, *Understanding Molecular Simulation*, 2nd ed. (Academic, New York, 2002).
- <sup>62</sup>H. J. C. Berendsen, J. P. M. Postma, W. F. van Gunsteren, and J. Hermans, in *Intermolecular Forces*, edited by B. Pullman (D. Reidel Publishing Company, Dordrecht, 1981), p. 331.
- <sup>63</sup>H. J. C. Berendsen, J. R. Grigera, and T. P. Straatsma, *J. Phys. Chem.* **91**, 6269 (1987).
- <sup>64</sup>D. Van Der Spoel, E. Lindahl, B. Hess, G. Groenhof, A. E. Mark, and H. J. C. Berendsen, *J. Comput. Chem.* **26**, 1701 (2005).
- <sup>65</sup>T. Darden, D. York, and L. Pedersen, *J. Chem. Phys.* **98**, 10089 (1993).
- <sup>66</sup>B. Hess, H. Bekker, H. J. C. Berendsen, and J. G. E. M. Fraaije, *J. Comput. Chem.* **18**, 1463 (1997).
- <sup>67</sup>J. P. Ryckaert, G. Ciccotti, and H. J. C. Berendsen, *J. Comput. Phys.* **23**, 327 (1977).
- <sup>68</sup>S. Miyamoto and P. Kollman, *J. Comput. Chem.* **13**, 952 (1992).
- <sup>69</sup>I.-C. Yeh and M. L. Berkowitz, *J. Chem. Phys.* **111**, 3155 (1999).
- <sup>70</sup>J. Janček, H. Krienke, and G. Schmeer, *J. Phys. Chem. B* **110**, 6916 (2006).
- <sup>71</sup>T. R. Jensen, M. Ø. Jensen, N. Reitzel, K. Balashev, G. H. Peters, K. Kjaer, and T. Bjørnholm, *Phys. Rev. Lett.* **90**, 086101 (2003).
- <sup>72</sup>M. Ø. Jensen, O. G. Mouritsen, and G. H. Peters, *J. Chem. Phys.* **120**, 9729 (2004).
- <sup>73</sup>A. Pertsin and M. Grunze, *J. Chem. Phys.* **125**, 114707 (2006).
- <sup>74</sup>M. J. de Ruijter, T. D. Blake, and J. De Coninck, *Langmuir* **15**, 7836 (1999).
- <sup>75</sup>J. S. Huang and W. W. Webb, *J. Chem. Phys.* **50**, 3677 (1969).
- <sup>76</sup>D. Beysens and M. Robert, *J. Chem. Phys.* **87**, 3056 (1987).
- <sup>77</sup>D. M. Huang, C. Sendner, D. Horinek, R. R. Netz, and L. Bocquet (unpublished).
- <sup>78</sup>W. R. P. Scott *et al.*, *J. Phys. Chem. A* **103**, 3596 (1999).
- <sup>79</sup>W. L. Jorgensen, J. D. Madura, and C. J. Swenson, *J. Am. Chem. Soc.* **106**, 6638 (1984).
- <sup>80</sup>W. L. Jorgensen, *J. Phys. Chem.* **90**, 1276 (1986).
- <sup>81</sup>K. C. Hass, W. F. Schneider, A. Curioni, and W. Andreoni, *J. Phys. Chem. B* **104**, 5527 (2000).
- <sup>82</sup>M. Flörsheimer, K. Kruse, R. Polly, A. Abdelmonem, B. Schimmelpfennig, R. Klenze, and T. Fanghänel, (unpublished).
- <sup>83</sup>P. Jungwirth and D. J. Tobias, *Chem. Rev. (Washington, D.C.)* **106**, 1259 (2006).
- <sup>84</sup>T. M. Chang and L. X. Dang, *Chem. Rev. (Washington, D.C.)* **106**, 1305 (2006).
- <sup>85</sup>J. Rowlinson and B. Widom, *Molecular Theory of Capillarity* (Oxford University Press, Oxford, 1982).
- <sup>86</sup>W. L. Jorgensen, D. S. Maxwell, and J. Tirado-Rives, *J. Am. Chem. Soc.* **118**, 11225 (1996).
- <sup>87</sup>W. D. Cornell *et al.*, *J. Am. Chem. Soc.* **117**, 5179 (1995).
- <sup>88</sup>J. Alejandre, D. J. Tildesley, and G. A. Chapela, *J. Chem. Phys.* **102**, 4574 (1995).
- <sup>89</sup>D. Paschek, *J. Chem. Phys.* **120**, 6674 (2004).
- <sup>90</sup>D. Horinek and R. R. Netz, *Phys. Rev. Lett.* **99**, 226104 (2007).
- <sup>91</sup>D. Horinek, A. Serr, D. J. Bonthuis, M. Boström, W. Kunz, and R. R. Netz, *Langmuir* **24**, 1271 (2008).
- <sup>92</sup>E. Lauga, M. P. Brenner, and H. A. Stone, in *Handbook of Experimental Fluid Dynamics*, edited by C. Tropea, A. Yarin, and J. F. Foss (Springer, New York, 2005).
- <sup>93</sup>L. Bocquet and J. L. Barrat, *Soft Matter* **3**, 685 (2007).
- <sup>94</sup>J. Chowdhary and B. Ladanyi, *J. Phys. Chem. B* **110**, 15442 (2006).
- <sup>95</sup>M. L. Berkowitz and K. Raghavan, *Langmuir* **7**, 1042 (1991).
- <sup>96</sup>A. Serr, D. Horinek, and R. R. Netz, *J. Am. Chem. Soc.* **130**, 12408 (2008).
- <sup>97</sup>D. Horinek *et al.*, *Proc. Natl. Acad. Sci. U.S.A.* **105**, 2842 (2008).